

Article

Hydrodynamic Performance Assessment of Emerged, Alternatively Submerged and Submerged Semicircular Breakwater: An Experimental and Computational Study

Faris Ali Hamood Al-Towayti ^{1,*}, Hee-Min Teh ^{1,2,*}, Zhe Ma ³, Idris Ahmed Jae ⁴ , Agusril Syamsir ⁴ 
and Ebrahim Hamid Hussein Al-Qadami ⁵

¹ Department of Civil and Environmental Engineering, Universiti Teknologi PETRONAS, Seri Iskandar 32610, Perak, Malaysia

² Institute of Self-Sustainable Building, Universiti Teknologi PETRONAS, Seri Iskandar 32610, Perak, Malaysia

³ State Key Laboratory of Coastal and Offshore Engineering, Dalian University of Technology, Dalian 116024, China; deep_mzh@dlut.edu.cn

⁴ Institute of Energy Infrastructure, Universiti Tenaga Nasional, Putrajaya Campus, Jalan IKRAM-UNITEN, Kajang 43000, Selangor, Malaysia; idris.ahmad@uniten.edu.my (I.A.J.); agusril@uniten.edu.my (A.S.)

⁵ Eco Hydrology Technology Research Centre (Eco-Hytech), Faculty of Civil Engineering and Built Environment, Universiti Tun Hussein Onn Malaysia, Parit Raja 86400, Johor, Malaysia; ebrahim@uthm.edu.my

* Correspondence: faris_18000464@utp.edu.my (F.A.H.A.-T.); heemin.teh@utp.edu.my (H.-M.T.)

Abstract: Coastal protection structures are essential defenses against wave energy, safeguarding coastal communities. This study aims to refine coastal protection strategies by employing a semicircular breakwater (SBW) model. Through a combination of physical and computational models, the hydrodynamic properties of the SBW under regular wave conditions were thoroughly examined. The primary objectives included delineating the hydrodynamic characteristics of SBWs, developing a computational model to validate experimental findings. Hydrodynamic characteristics of the SBW model were scrutinized across various wave conditions. Experimental testing in a wave flume covered a range of relative water depths (d/h) from 0.667 to 1.667, wave steepness (H_i/L) spanning 0.02 to 0.06 and wave periods ranging from 0.8 to 2.5 s. Notably, analysis of an emerged SBW with $d/h = 0.667$ revealed superior wave reflection, while an alternative submerged SBW with $d/h = 1.000$ showed the highest energy loss. These findings are further corroborated by the validation of computational models against experimental outcomes for $d/h = 0.667, 1.000, 1.333$ and 1.667 . Moreover, the investigation of forces revealed an inverse correlation between horizontal forces and wave height, while vertical forces showed nuanced variations, including a slightly decreasing average vertical force with greater relative wave period (B/L) for different immersion scenarios.

Keywords: semicircular breakwater; hydrodynamic performance; experimental model; computational model; horizontal forces; vertical forces; mangrove ecosystems



Citation: Al-Towayti, F.A.H.; Teh, H.-M.; Ma, Z.; Jae, I.A.; Syamsir, A.; Al-Qadami, E.H.H. Hydrodynamic Performance Assessment of Emerged, Alternatively Submerged and Submerged Semicircular Breakwater: An Experimental and Computational Study. *J. Mar. Sci. Eng.* **2024**, *12*, 1105. <https://doi.org/10.3390/jmse12071105>

Received: 15 May 2024

Revised: 19 June 2024

Accepted: 25 June 2024

Published: 29 June 2024



Copyright: © 2024 by the authors. Licensee MDPI, Basel, Switzerland. This article is an open access article distributed under the terms and conditions of the Creative Commons Attribution (CC BY) license (<https://creativecommons.org/licenses/by/4.0/>).

1. Introduction

Coastal protection is crucial for ensuring the safety and sustainability of communities and maritime activities. Breakwaters are essential structures designed to mitigate the impact of waves and currents, reduce wave heights and prevent wave-induced erosion [1]. They are built in various shapes and sizes using materials such as concrete, rocks or steel, depending on specific coastal conditions [2]. Three main types of breakwaters are commonly used: vertical, rubble mound and composite breakwaters [3]. Rubble mound breakwaters are the most effective in dissipating wave energy, while vertical breakwaters reflect the maximum wave energy but disperse only a limited amount [4]. Composite breakwaters use a combination of components to reflect and dissipate wave energy through a semi-circular caisson, providing an efficient and stable option for coastal protection [5]. Among the different types of breakwaters, semicircular breakwaters offer

several advantages such as efficient wave energy dissipation, stability from the semi-circular caisson design, cost-effectiveness and a visually pleasing appearance [6–8]. Designing breakwaters is challenging due to harsh wave environments and poor ground conditions [9]. Despite the challenges, breakwaters are crucial for providing a safe and stable environment for maritime activities, while safeguarding coastal communities [10].

Mangroves, thriving in saline coastal environments, play a vital role in mitigating coastal erosion, protecting against storm surges and stabilizing shorelines through their intricate root systems [11]. Between 2000 and 2014, mangrove forests worldwide shrank from 137,760 km² to 81,484 km² due to human activity, despite their importance as green infrastructure [12,13]. This loss significantly contributes to climate change, given mangroves' high carbon sequestration capacity [14]. Efforts to restore mangrove forests have been undertaken globally, driven by policies from government, non-government and nonprofit organizations [12,15]. However, restoration projects often fall short of expectations and even fail due to a range of challenges, including physical and biological factors, emphasizing the need for innovative approaches to preserve mangroves while ensuring coastal protection [16–18].

Due to recent advancements in design and construction, several new model designs have been implemented [19,20]. One concept is the SBW which is focused on by several researchers in China and Japan [6]. The SBW has a semi-circular caisson and bottom slab which is placed on a prepared rubble mound [21]. SBW has been categorized into four types: solid, permeable, front dissipation and rear dissipation [22]. Figure 1 illustrates these distinct SBW types. The SBW offers several advantages, including high stability in the presence of wave action due to its circular shape and the minimization of vertical forces on the foundation due to its hollow structure [23].

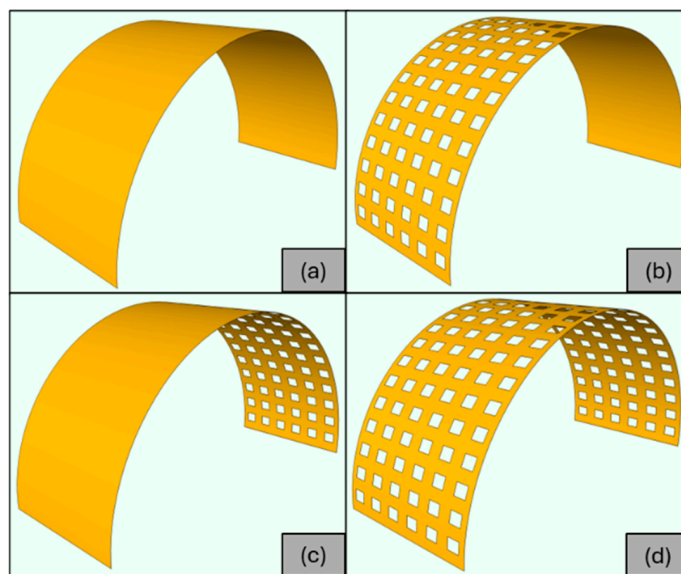


Figure 1. Types of SBWs—(a) solid SBW, (b) front side SBW, (c) rear side SBW, (d) fully perforated SBW.

The study of SBWs began in the 1980s with Tanimoto and his research team [24,25]. Large-scale reinforced concrete structure SBWs with a semicircular caisson and a bottom slab made of precast were previously built at China's Yangtze Estuary, Japan's Miyazaki Port, Vietnam's Nha Mat Bac Place and China's Tianjin Port [26–28]. Prior research on coastal structures of this nature primarily focused on assessing hydrodynamic variables, including pressure, reflection, transmission and energy loss coefficients, wave diffraction, rundown, runup and factors associated with energy dissipation by the SBW. Several semi-empirical design formulas have been proposed [29–31].

Field tests have been conducted on SBWs constructed in the port of Miyazaki. The wave pressure data were reported to confirm a decrease in the horizontal force component,

enhancing the structure's ability against sliding [32]. Prior research on SBWs featured finite element models, offering detailed analyses of structural behavior and performance [33]. To compute the pressures on the SBW, wave pressures were measured at various heights on the structure. The pressure decreased dynamically and exponentially from the water surface to the bed with increased wavelength and a lower immersion depth. Additionally, it was observed that Goda's modified approach accurately calculated the pressure magnitude, especially near the Stillwater level [34]. Another study found that the modified Goda method tends to underpredict the pressure at relative depth (d/L) < 0.35 and overpredict the pressure on impermeable structures at $d/L > 0.58$, where d is the water depth and L is the wavelength [35]. Investigating how differences in rubble mound height, water depth and perforation percentage affect the ability of semicircular breakwaters to convert non-breaking waves [36].

The interaction between the wave and the cylinder was studied using physical and computational modelling [37]. The equivalence of wave height on the porous cylinder to that of incident waves was observed. Investigations were carried out on models of emerged breakwaters with and without perforations. The findings revealed that an increase in the height and inclination of the incident waves resulted in a higher reflection coefficient [38]. Another study [39] examined the impact of submerged vertical and SBWs on local wave characteristics, specifically focusing on determining wave reflection coefficients. The proposed semi-empirical parameterizations rely on the dimensionless submergence parameter a/H (a —the depth of submergence of the breakwater; H_i —the height of the incident wave at the breakwater).

A recent study investigated the critical weight required to ensure sliding stability. Various parameters, including water depth and wave characteristics, were considered. A physical model of emerged and perforated (SBW) facing waves was utilized. The study also established a correlation between the hole diameter and spacing. Results showed that the stability parameter decreased with an increase in the slope of wave incident across all depth parameter ranges. Additionally, the study revealed a positive correlation between SBW stability and water depth, where an increase in the depth parameter led to a higher minimum weight required to maintain stability in sliding [40].

Analysis of this kind of structure using computational models has been made possible by the emergence of tools for Computational Fluid Dynamics (CFD) modelling, in tandem with the rise in processing capacity. Computational simulations can be utilized to investigate the interaction between breakwaters and fluids, thereby facilitating the assessment of wave loads on intricate geometric breakwaters. Flow-3D has been widely used in various fluid–structure interaction studies related to coastal structures, such as breakwater armour arrangements, concrete armoured blocks and floating breakwaters. According to their findings, the Volume of Fluids (VOF) algorithm-based computational method performed better than other computational codes [41]. Utilizing Flow-3D[®] v11.2 software, an assessment was conducted to evaluate the effectiveness of various shapes of concrete armored blocks in the context of breakwaters [42]. Conducting a study that combines Flow-3D software and a physical model to analyze the performance of a floating breakwater [43], researchers demonstrated the software's capability to accurately simulate hydrodynamic interaction effects with the analyzed structure.

This research aims to identify the hydrodynamic characteristics of emerged, submerged and alternatively submerged small-scale SBWs and establish a computational model to authenticate the experimental findings. By substituting geotextile tubes with durable SBWs, the study addresses drawbacks such as short lifespan and susceptibility to punctures. SBWs provide a sustainable solution for safeguarding mangrove ecosystems and have wide-ranging applications in coastal protection. The insights obtained contribute to bolstering coastal resilience and promoting biodiversity conservation under regular wave conditions. The comprehensive model takes into account variables such as water depth and wave periods, aligning with prevalent conditions in regions like Malaysia. The paper is organized as follows: Section 1 outlines the objectives and background; Section 2

elaborates on the methodology, including the setup of the computational model for validation; Section 3 discusses an analytical error analysis; Section 4 presents the results and discussion, juxtaposing computational findings with experimental data to validate the model; and Section 5 summarizes the conclusions and key finding.

2. Methodology

The procedure described in this study involves two phases: the experimental phase and the computational phase. In the experimental phase, a physical model of the SBW is constructed and tested in a wave tank to measure its hydrodynamic responses to different wave conditions. The aim is to compute the transmission coefficient (C_T), reflection coefficient (C_R) and energy loss coefficient (C_L). In the computational phase, a computational model of the SBW is created using Flow-3D software and simulated under various wave conditions. The results of the physical tests and computational simulations are analyzed to evaluate the performance of the SBW in reducing the height of the waves.

2.1. Description of Experimental Setup

The study utilized an SBW model that was built with specific dimensions to evaluate its hydraulic characteristics under different wave conditions. The model had an external radius (R) of 0.6 m, a thickness of 0.1 m and a length of 0.8 m. The width of the SBW (B) was 1.2 m, while the height (h) was the same as R . To ensure that the model accurately matched the geometrical requirements of the test facility, a Froude scaling ratio of 1:2.5 was employed. The model was constructed using concrete material with a density of 2400 kg/m^3 , as shown in Figure 2. The experiment was conducted at the Offshore Laboratory in Universiti Teknologi PETRONAS. It featured a wave generator integrated into a flume, with a shallow basin with a maximum water depth of 1 m and a length of 20 m. Waves were generated and directed towards the SBW model, positioned 10 m away from the wave generator at one end of the flume. Six wave probes were strategically placed along the flume to measure water profiles. Offshore probes WP1, WP2 and WP3 captured reflected and incident waves, while shoreward probes WP4, WP5 and WP6 measured transmitted wave height.

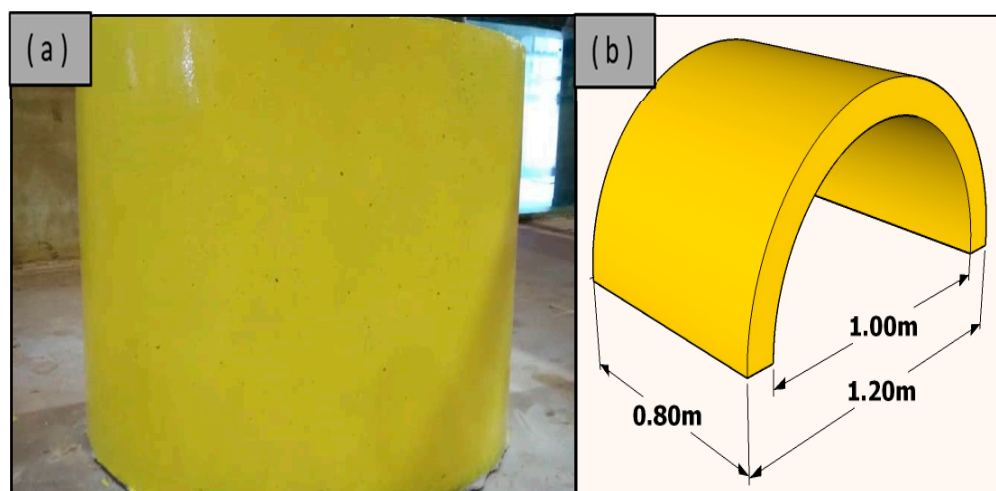


Figure 2. SBW Model: (a) photographic representation and (b) schematic illustration with dimensional annotations.

In configuring the experimental setup, the lateral side of the SBW was meticulously sealed using silicon and cement to prevent any gaps. Additional trials confirmed the effectiveness of this sealing, ensuring no waves breached through the sealed gap and that the results remained unaffected. To mitigate reflections, the experimental setup employed a piston-type active absorbing wavemaker system, renowned for its absorption capability exceeding 96.5% at target wave fields [44]. This system actively absorbs waves, minimizing spurious reflections from the wavemaker. Complementary passive absorption mechanisms

prevent wave reflection from fixed boundaries within the flume [45]. Absorbing wavemakers offer dynamic cancellation of re-reflective waves by adjusting paddle motion, with a specially designed controller proving effective for both regular and irregular waves [46]. Hydrodynamic feedback signals are integrated into paddle control to eliminate re-reflection of waves generated by the wavemaker [47]. Furthermore, optimization of parameters for the absorbing beach in the wave tank significantly reduces reflection from the beach, ensuring accurate measurements [48].

The SBW model was tested with wave steepness values of 0.02, 0.04 and 0.06, alongside varying relative water depth parameters (d/h) of 0.667, 1.000, 1.333 and 1.667 under regular wave conditions. Before the experiment, all wave probes underwent meticulous calibration. A wave absorber was strategically placed at the end of the flume to nullify incoming waves effectively. This structure minimized wave reflection from the end wall during experiments by featuring a 1:10 slope and comprised of right-angle triangular-shaped structures, each filled with filtering materials and covered by a steel grating to enhance efficiency. A total of 216 experiments were conducted using the least-squares approach of Mansard and Funke.

Table 1 presents the experimental and computational parameters, including the wave steepness (H_i/L), relative water depth (d/h , where d is water depth and h is SBW height), relative wave period (B/L where B is SBW width and L is wavelength) [49] and the total number of the experiments conducted. Figure 3 illustrates the laboratory setup through both a photograph and a schematic with components. Figure 4 presents photographs of the laboratory setup at various d/h ratios. Figure 5 delves into a comparative time series analysis of wave data at designated measurement points for various d/h ratios (a) $d/h = 0.667$, (b) $d/h = 1.000$, (c) $d/h = 1.333$ and (d) $d/h = 1.667$, with wave period 1.6 and wave steepness 0.02.

Table 1. Scope of experimental and computational parameters.

| Wave-Specific Parameters | Range |
|-------------------------------------|-------------------------------|
| Height of incident waves, H_i (m) | 0.02–0.38 |
| Water depth, d (m) | 0.4, 0.6, 0.8 and 1.0 |
| Wave period, T (s) | 0.8–2.5 ($DT = 0.1$ s) |
| Wave steepness H_i/L | 0.02, 0.04, 0.06 |
| Relative water depth, d/h | 0.667, 1.000, 1.333 and 1.667 |
| Relative wave period, B/L | 0.17–1.22 |

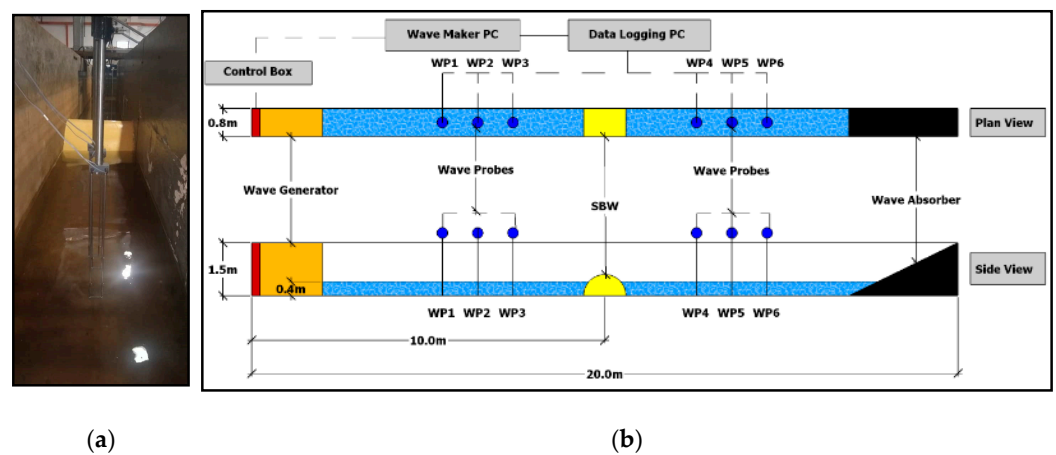


Figure 3. Laboratory setup: (a) photo of setup, (b) schematic with components.

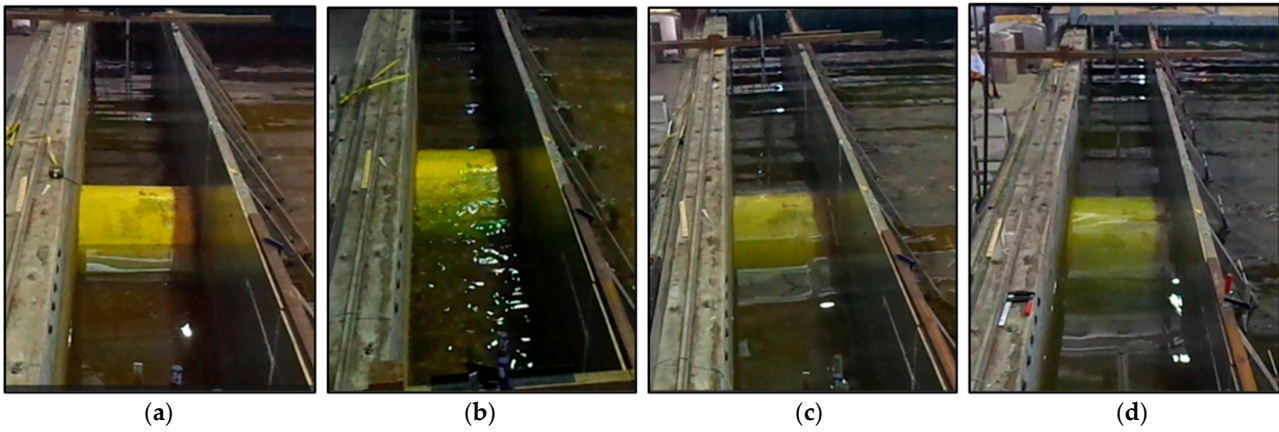


Figure 4. Photograph of laboratory setup at (a) $d/h = 0.667$, (b) $d/h = 1.000$ and (c) $d/h = 1.333$, (d) $d/h = 1.667$.

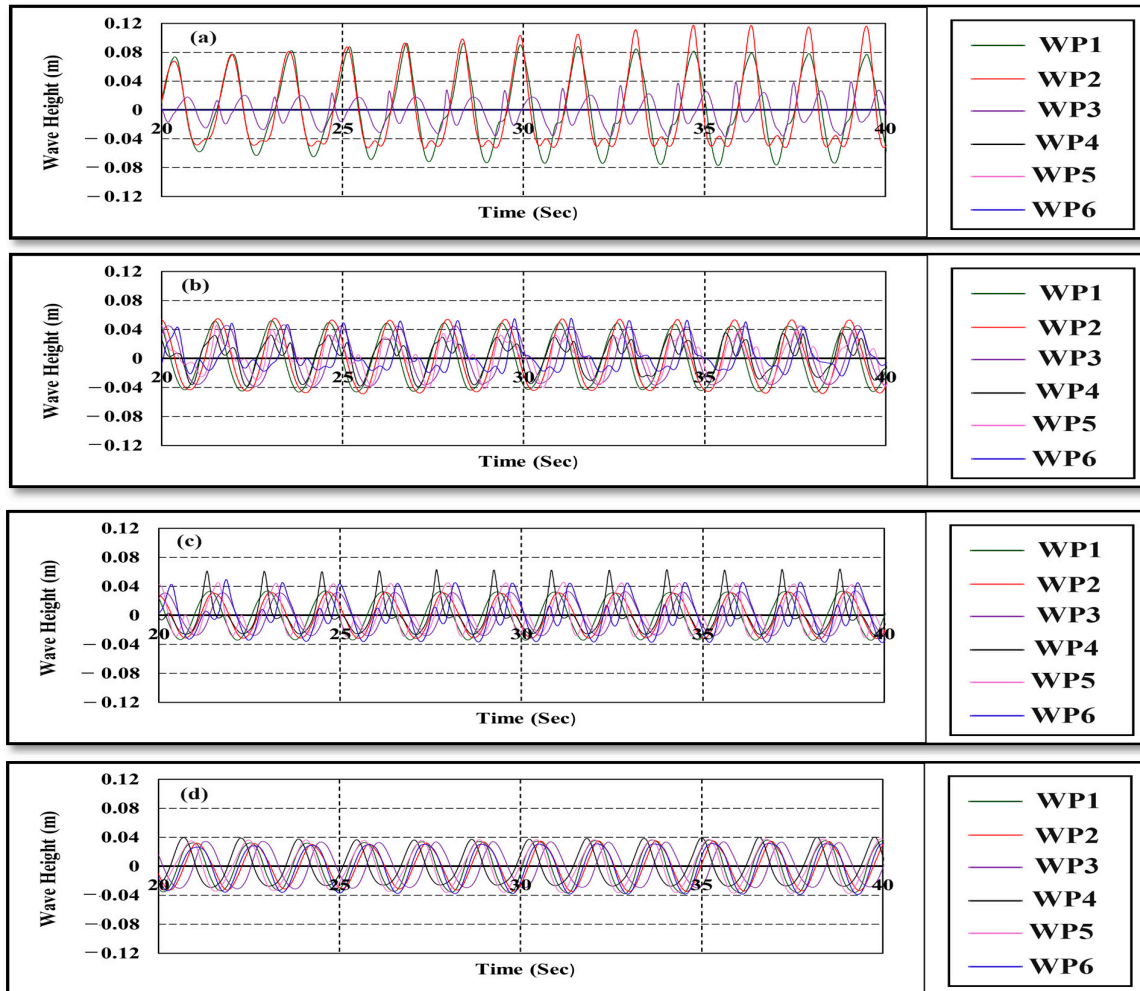


Figure 5. Comparative time series analysis of wave data at measurement points for various d/h ratios (a) $d/h = 0.667$, (b) $d/h = 1.000$, (c) $d/h = 1.333$ and (d) $d/h = 1.667$.

2.2. Description of Computational Modeling Approach

The research utilized commercial computational fluid dynamics (CFD) software called Flow-3D to perform the computational runs. Flow-3D uses the Volume of Fluid (VOF) algorithm to model free surface flows [50] and wave structure interactions in coastal

engineering [51]. VOF tracks the interface between fluids, which is governed by partial differential equations [52]. While CFD allows detailed simulations of coastal dynamics, its accuracy depends on data quality and field validation due to the complex nature of coastal environments.

2.2.1. Governing Equations

To simulate fluid flows in three-dimensional form, the mass continuity and Navier–Stokes momentum equations were used for incompressible fluids, within the Cartesian coordinate system [53]. The mass continuity equation is initially presented in Equation (1). However, for simulating incompressible fluid flow, this equation can be simplified, as shown in Equation (2). Meanwhile, Navier–Stokes equations were employed to solve the fluid velocity components (u, v, w) in the (x, y, z) directions. Equations (3)–(5) illustrate the general forms of the momentum equations utilized in Flow-3D for simulating incompressible fluid dynamics using Cartesian coordinates.

$$V_F \frac{\partial \rho}{\partial t} + \frac{\partial}{\partial x}(\rho u A_x) + R \frac{\partial}{\partial y}(\rho v A_y) + \frac{\partial}{\partial z}(\rho w A_z) + \xi \frac{\rho u A_x}{x} = R_{DIF} + R_{SOR} \quad (1)$$

$$\frac{\partial u A_x}{\partial x} + R \frac{\partial v A_y}{\partial y} + \frac{\partial w A_z}{\partial z} + \xi \frac{u A_x}{x} = \frac{R_{SOR}}{\rho} \quad (2)$$

$$\frac{\partial u}{\partial t} + \frac{1}{V_F} \left\{ u A_x \frac{\partial u}{\partial x} + v A_y R \frac{\partial u}{\partial y} + w A_z \frac{\partial u}{\partial z} \right\} - \xi \frac{A_y v^2}{x V_F} = -\frac{1}{\rho} \frac{\partial P}{\partial x} + G_x + f_x - b_x - \frac{R_{SOR}}{\rho V_F} (u - u_w - \delta u_s) \quad (3)$$

$$\frac{\partial v}{\partial t} + \frac{1}{V_F} \left\{ u A_x \frac{\partial v}{\partial x} + v A_y \frac{\partial v}{\partial y} + w A_z \frac{\partial v}{\partial z} \right\} + \xi \frac{A_y u v}{x V_F} = -\frac{1}{\rho} \left(R \frac{\partial P}{\partial y} \right) + G_y + f_y - b_y - \frac{R_{SOR}}{\rho V_F} (v - v_w - \delta v_s) \quad (4)$$

$$\frac{\partial w}{\partial t} + \frac{1}{V_F} \left\{ u A_x \frac{\partial w}{\partial x} + v A_y R \frac{\partial w}{\partial y} + w A_z \frac{\partial w}{\partial z} \right\} = -\frac{1}{\rho} \frac{\partial P}{\partial z} + G_z + f_z - b_z - \frac{R_{SOR}}{\rho V_F} (w - w_w - \delta w_s) \quad (5)$$

where V_F is the fractional volume open to flow, ρ is the fluid density, R_{DIF} is a turbulent diffusion term, R_{SOR} is a mass source term and P denotes the pressure. The vectors (G_x, G_y, G_z) represent body accelerations, (f_x, f_y, f_z) are viscous accelerations and (b_x, b_y, b_z) account for flow losses in porous media or across porous baffle plates. Additionally, the final terms account for the injection of mass at a source represented by a geometry component. Lastly, P denotes the pressure.

As mentioned earlier, the Flow-3D solver detected the flow free surface using the VOF function. The VOF technique has three main components: defining the VOF function, solving the VOF transport equation (Equations (6) and (7)) and setting the boundary conditions at the free surface. The VOF method, based on the concept of a fractional volume of fluid, is more flexible and efficient for treating complicated free boundary configurations in numerical simulations [54]. In one-fluid simulations using Flow-3D, the volume-of-fluid (VOF) function (F) is essential for delineating fluid presence within computational cells. Void cells, indicated by ($F = 0$), represent regions devoid of fluid where variations in pressure, temperature, inertia and friction at the fluid interface are negligible, typically found in scenarios where gas density is significantly lower than that of the fluid and gas velocity matches fluid velocity. This approach efficiently models free surfaces in applications like mold filling with liquid metal, water flow in rivers and micro-fluidic devices, circumventing the computational expense of explicitly modeling gas flow [55]. (F) signifies fluid volume: ($F = 1$) for fully filled cells and ($0 < F < 1$) for partially filled cells, crucial for accurate simulation of complex boundaries and free surface phenomena [55,56]. In this range, the variable (F) quantifies the fraction of the cell volume that is occupied by the fluid, allowing for a detailed representation of the varying degrees of fluid presence within the computational grid, as demonstrated in Figure 6.

$$\frac{\partial F}{\partial t} + \frac{1}{V_F} \left[\frac{\partial}{\partial x}(F A_x u) + R \frac{\partial}{\partial y}(F A_y v) + \frac{\partial}{\partial z}(F A_y w) + \xi \frac{F A_x u}{x} \right] = F_{DIF} + F_{SOR} \quad (6)$$

$$F_{DIF} = \frac{1}{V_F} \left\{ \frac{\partial}{\partial x} \left(v_F A_x \frac{\partial F}{\partial x} \right) + R \frac{\partial}{\partial x} \left(v_F A_y R \frac{\partial F}{\partial y} \right) + \frac{\partial}{\partial z} \left(v_F A_z \frac{\partial F}{\partial z} \right) + \zeta \frac{v_F A_x F}{x} \right\} \quad (7)$$

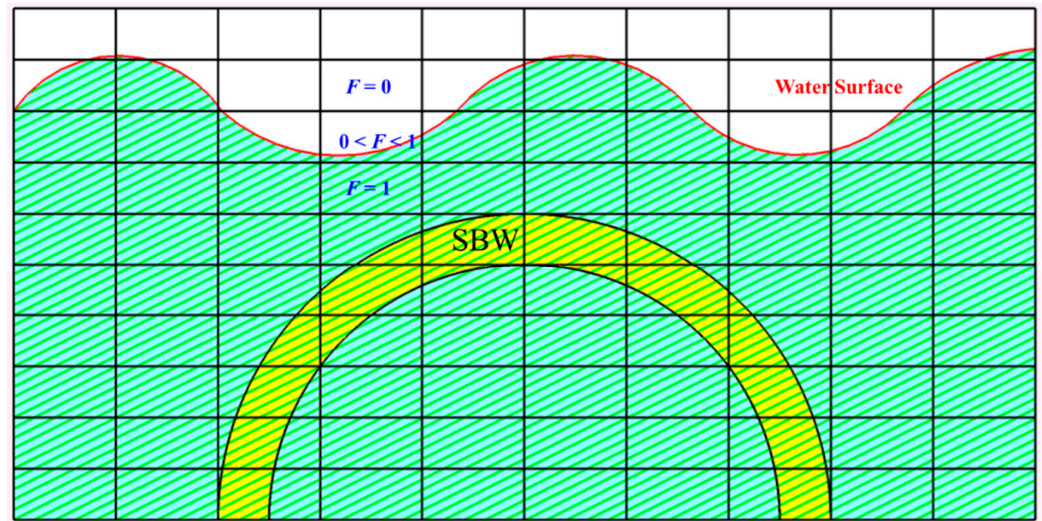


Figure 6. Two-dimensional view of SBW with integrated free surface via volume of fluid function at $d/h = 1.333$.

The fractional volume open to flow (V_F) is influenced by fluid density (ρ), velocity components (u, v, w) in specific coordinate directions, fractional area open to flow (A_x, A_y, A_z) in corresponding directions, density source term (R_{SOR}), turbulence diffusion term (R_{DIF}) and coefficients (R and ζ) dependent on the coordinate system. When using cylindrical coordinates, y derivatives are converted to azimuthal derivatives, and ζ is set to 1. For Cartesian coordinates, R is set to unity, and ζ is set to zero.

To model turbulence in this study, the widely recognized two-equation $k-\epsilon$ model was employed, which is among the most advanced equations commonly used for fluid engineering [57–59]. This turbulence model utilizes two transport equations, one for turbulent kinetic energy (k) and another for its dissipation (ϵ). The turbulent kinetic energy represents the energy associated with the turbulent variations in fluid flow, while the dissipation rate quantifies the rate at which this energy is dissipated as turbulence is attenuated. When using the $K-\epsilon$ turbulence model, the boundary condition on the SBW’s surface was set to be no slip, and the maximum turbulent mixing length was chosen to be dynamically calculated using the algorithm of Flow-3D software. By incorporating these transport equations, the study aimed to accurately simulate and analyze the wave characteristics within the fluid flow surrounding the SBW under investigation. The two-equation $k-\epsilon$ turbulence model is widely regarded as a sophisticated and extensively employed model for solving turbulent flows. Its versatility has been demonstrated in providing reasonable approximations for various types of flows [53].

2.2.2. Computational Model

The computational model developed for simulating SBW hydrodynamics using Flow-3D is illustrated in Figure 7. This figure is made up of five sub-figures that depict specific configurations of the breakwater at varying depths. They are (a) setup and mesh, (b) $d/h = 0.667$ emerged, (c) $d/h = 1.000$ alternately submerged, (d) $d/h = 1.333$ and (e) $d/h = 1.667$ fully submerged SBWs. The computational mesh is carefully designed with varied cell sizes of 0.04 m for the flume and 0.01 m for the SBW, to align with the experimental parameters and balance resolution and computational efficiency as shown in Table 2. SolidWorks-crafted SBW geometry in STL format is integrated into the model to ensure seamless representation. To optimize computational efficiency while preserving experimental relevance, a 0.04 m strip was extracted from the 0.8 m width. At the left boundary, the incident wave conditions were applied, while at the right boundary, an absorption

boundary was used to avoid wave reflection. Symmetry conditions were utilized for all other open boundaries. Figure 8 shows the time step size used by the Flow-3D solver on selected mesh sizes for SBW simulation.

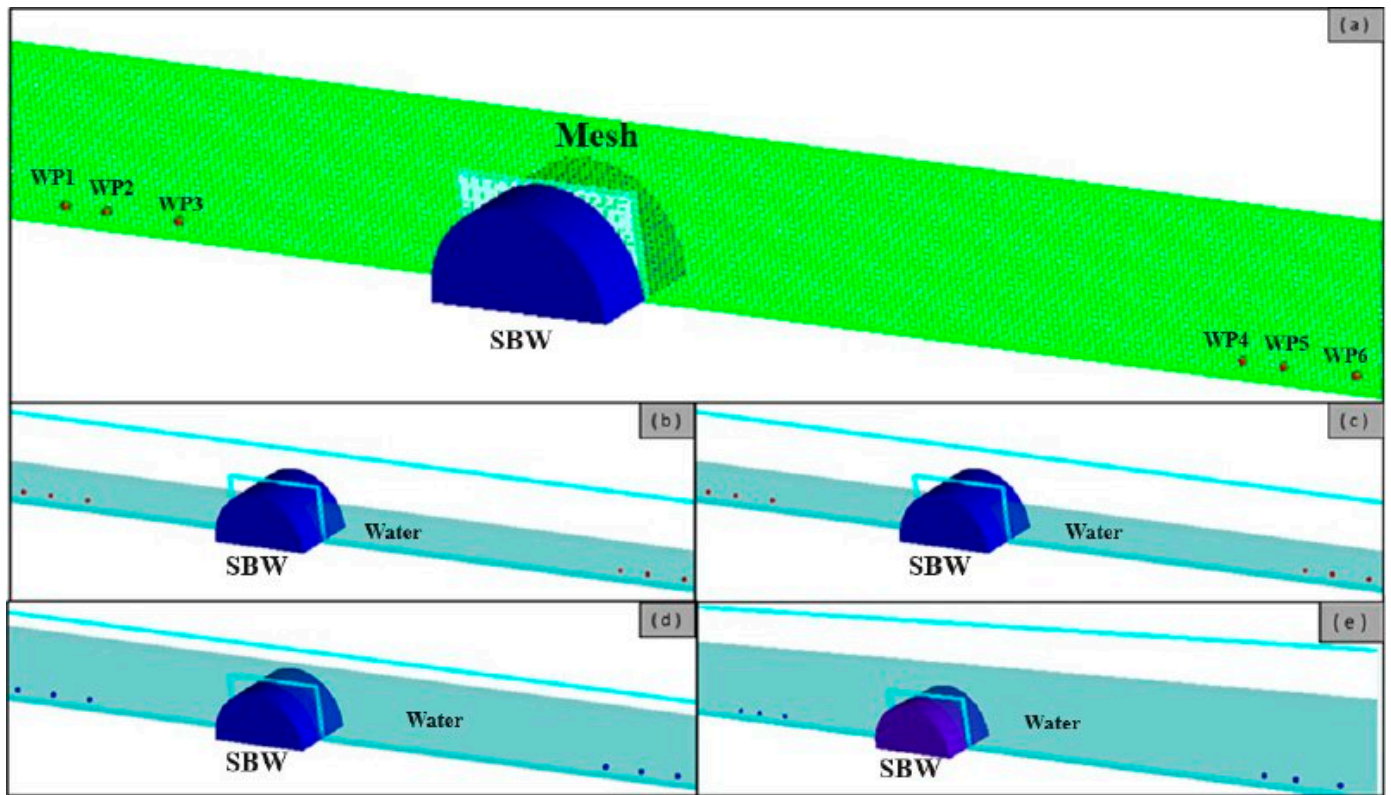


Figure 7. Computational model (a) setup and mesh, (b) $d/h = 0.667$, (c) $d/h = 1.000$, (d) $d/h = 1.333$, (e) $d/h = 1.667$.

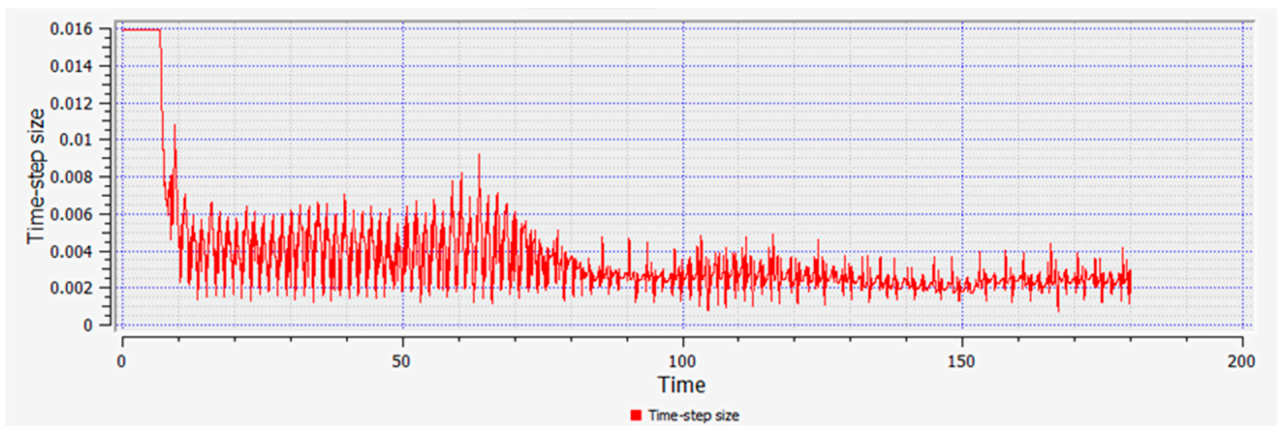


Figure 8. Time step size utilized by Flow-3D solver on selected mesh size for SBW simulation.

Table 2. Average flow velocity and Froude number values at different cell sizes (0.01 m to 0.1 m) for SBW simulation at steady state.

| Cell Size (m) | 0.1 | 0.08 | 0.06 | 0.04 | 0.03 | 0.02 | 0.01 |
|---------------------|-------|-------|-------|-------|-------|-------|-------|
| Flow Velocity (m/s) | 0.034 | 0.034 | 0.033 | 0.035 | 0.038 | 0.038 | 0.38 |
| Froud Number | 0.066 | 0.064 | 0.063 | 0.068 | 0.073 | 0.072 | 0.072 |

2.3. Performance Evaluation Measurements

The assessment of SBW performance commonly involves the use of transmission coefficient (C_T), reflection coefficient (C_R) and energy dissipation coefficients (C_L) [60]. These coefficients are expressed mathematically as:

$$C_T = \frac{H_T}{H_i} \tag{8}$$

$$C_R = \frac{H_R}{H_i} \tag{9}$$

$$C_L = \sqrt{1 - (C_T^2 + C_R^2)} \tag{10}$$

In the equations, H_i , H_T and H_R represent the mean values of the incident, transmitted and reflected waves, respectively. Estimating energy dissipation at the breakwater poses a challenge due to its complexity in measurement [61–64], influenced by factors like relative submerge depth, crest width and wave slope [61]. Consequently, the law of conservation of energy, as illustrated by Equation (10), is employed to approximate the amount of energy loss.

3. Analytical Error Analysis

The coefficient of determination (R^2 or r-squared) in regression models, calculated using Equation (11), is used to validate experimental results through computational analysis. A higher R^2 value indicates a stronger correlation between the datasets, suggesting a better fit of the two outcomes [65]. Alongside R^2 , error functions like Mean Square Error (MSE), Root Mean Square Error ($RMSE$), Mean Absolute Deviation (MAD) and Mean Absolute Percentage Error ($MAPE$) (Equations (12)–(15)) assess disparities between experimental and computational results [66–68]. These metrics play a critical role in evaluating computational model performance in validating experimental results, with smaller $RMSE$ and $MAPE$ values indicating closer agreement between experimental and computational values, signifying more accurate representation of experimental data by computational models. Thus, analyzing these error functions is essential for assessing computational model accuracy and reliability in validating experimental results.

$$R^2 = 1 - \frac{\sum_{i=1}^n (M_t - A_t)^2}{\sum_{i=1}^n (M_t - A_t)} \tag{11}$$

$$MSE = \frac{1}{n} \sum_{i=1}^n (A_t - M_t) \tag{12}$$

$$RMSE = \sqrt{\frac{1}{n} \sum_{i=1}^n (A_t - M_t)} \tag{13}$$

$$MAD = \frac{\sum_{i=1}^n |A_t - M_t|}{n} \tag{14}$$

$$MAPE = \frac{\sum_{i=1}^n \left| \frac{A_t - M_t}{A_t} \right|}{n} \tag{15}$$

where A_t represents experimental data, M_t represents computational data, A_X signifies the average of experimental data and n stands for the number of experiments conducted.

4. Results and Discussion

The experimental data, analyzed and portrayed through wave transmission, reflection and energy loss graphs, undergoes parallel scrutiny with computational model results for validation. These graphical representations establish correlations between wave characteristics (C_T , C_R and C_L) and horizontal and vertical forces, incorporating crucial dimensionless

parameters such as relative wave period (B/L), wave steepness (H_i/L) and relative water depth (d/h). Notably, this investigation spans four relative water depths— $d/h = 0.667, 1.000, 1.333$ and 1.667 —encompassing emerged, alternatively submerged and fully submerged configurations. In addition to wave transmission, reflection and energy loss graphs, the investigation includes analysis of wave forces on SBW, horizontal force analysis on SBW and vertical force analysis on SBW. The accuracy and reliability of the models are further evaluated through quantitative metrics, including MSE , $RMSE$, MAD , $MAPE$ and R^2 , offering a comprehensive understanding of model performance across diverse conditions. The forthcoming section will delve into the discussion of these mentioned graphs, providing detailed insights into the observed correlations and dynamics, as well as the effects of wave forces on the SBW structure, both horizontally and vertically. Figure 9 presents the free surface elevation comparison between the experimental (Exp) and computational (Comp) models at different d/h ratios: Figure 9a $d/h = 0.667$, Figure 9b $d/h = 1.000$, Figure 9c $d/h = 1.333$ and Figure 9d $d/h = 1.667$. This figure illustrates the agreement between the experimental and computational results for a wave period of 1.6 and a wave steepness of 0.02.

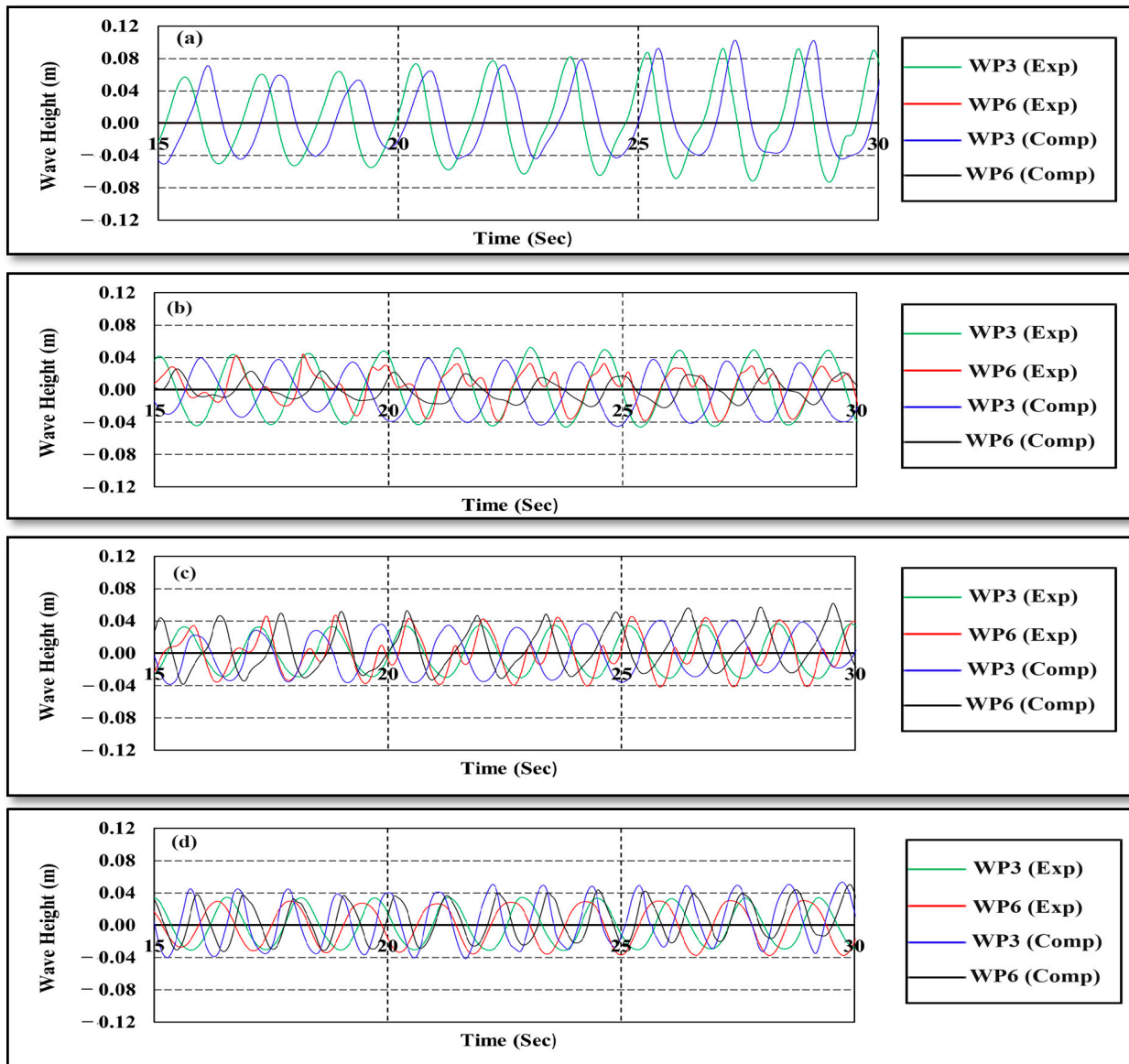


Figure 9. Free surface elevation comparison between (Exp) and (Comp) model at different d/h Ratios (a) $d/h = 0.667$, (b) $d/h = 1.000$, (c) $d/h = 1.333$, (d) $d/h = 1.667$.

4.1. Wave Transmission

In the examination of wave transmission, both experimental and computational analyses are undertaken to evaluate the SBW's capacity to convey wave energy. This assessment is primarily conducted through the wave transmission coefficient (C_T), which is defined as the ratio of wave height transmitted (H_T) to the height of the incident wave (H_i) [69–72]. A lower C_T value corresponds to increased wave attenuation by the SBW [69]. Figure 10 displays C_T values for $d/h = 0.667, 1.000, 1.333$ and 1.667 . In Figure 10a, the emerged SBW ($d/h = 0.667$) shows a decline in the transmission coefficient (C_T) with increasing B/L , regardless of H_i/L . This is consistent with previous studies which found that C_T decreases as B/L increases in cases with vertical structures [73] and a lower arc-plate breakwater [74]. C_T values at maximum and minimum, approximately 0.32 and 0, indicate enhanced wave attenuation with increasing B/L , particularly effective for intercepting shorter period waves when $B/L > 0.4$. The expanded SBW width facilitates more efficient interception and attenuation of waves with shorter wavelengths, carrying less energy and displaying less developed profiles. In Figure 10b, C_T for the alternatively submerged SBW ($d/h = 1.000$) declines with increasing B/L , irrespective of H_i/L . Recorded maximum and minimum C_T values are approximately 0.85 and 0.32, respectively. This suggests the alternatively submerged SBW's superior capability to intercept shorter-period waves during regular wave actions. Short waves, which convey lower energy flux and are less developed, undergo instability in the vicinity of the alternately submerged SBW. Certain waves have the potential to pass over, getting transmitted to the sheltered side of the structure with diminished wave height. In Figure 10c, for the fully submerged SBW with the relative water depth (d/h) of 1.333, C_T values exhibit relatively high values, ranging from 0.59 to 0.99, in comparison to those observed for the SBW with d/h ratios of 0.667 and 1.000. This implies that in comparison to the emerging and alternatively submerged SBW configurations, the submerged SBW exhibits less effective wave attenuation. The submerged SBW proves effective in intercepting longer period waves when B/L is less than 0.6. With shorter period waves, the size of the circular water particle orbits diminishes as the water column extends in the z-direction [75]. The influence of water particle orbits on the SBW is nearly negligible [76,77], enabling incident waves to pass through the submerged SBW with minimal flow interference. In Figure 10d, for the fully submerged SBW with d/h of 1.667, C_T values exhibit relatively high values ranging from 0.68 to 0.98 compared to other d/h values (0.667, 1.000 and 1.333), and C_T increases when B/L increases. In Figure 10, wave steepness significantly influences C_T for both $d/h = 0.667, 1.000, 1.333$ and 1.667 [78]. Similar findings from studies on submerged SBWs and rectangular breakwaters support this observation. The weaker effects of the submerged breakwater on waves result in higher C_T values in the numerical scheme, indicating that waves pass over the breakwater with minimal interaction [79]. C_T values decrease with increasing H_i/L for $d/h = 0.667, 1.333$ and 1.667 . In contrast, an inverse relationship is noted when (B/L) exceeds 0.5 for (d/h) equal to 1.000. During this phase, waves with higher steepness are partially intercepted by the SBW, and the remaining waves overtop the crest, forming transmitted waves of considerable sizes. Therefore, the C_T of higher steepness waves exhibits larger values.

Figures 11–13 validate the C_T for the SBWs across various H_i/L conditions. They illustrate C_T at low ($H_i/L < 0.02$), moderate ($0.02 < H_i/L < 0.04$) and high ($0.04 < H_i/L < 0.06$) wave steepnesses for different d/h ratios (0.667, 1.000, 1.333 and 1.667). These figures visually confirm the model's accuracy in predicting C_T , with computational results closely aligning with experimental data. Additionally, Table 3 presents a Comparative Analysis of Experimental and Computational Error Deviation Data for SBWs' C_T , providing essential metrics like—and R^2 across various H_i/L ratios and d/h scenarios.

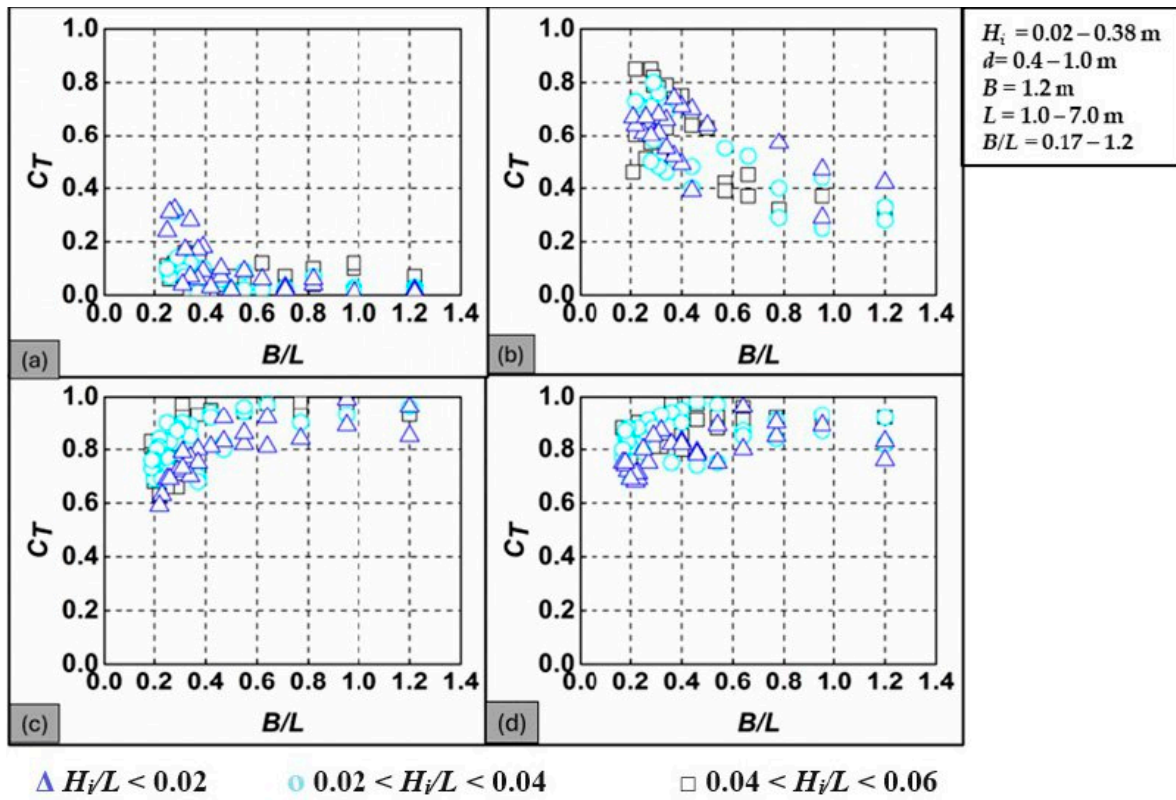


Figure 10. C_T of SBW—(a) $d/h = 0.667$, (b) $d/h = 1.000$, (c) $d/h = 1.333$, (d) $d/h = 1.667$.

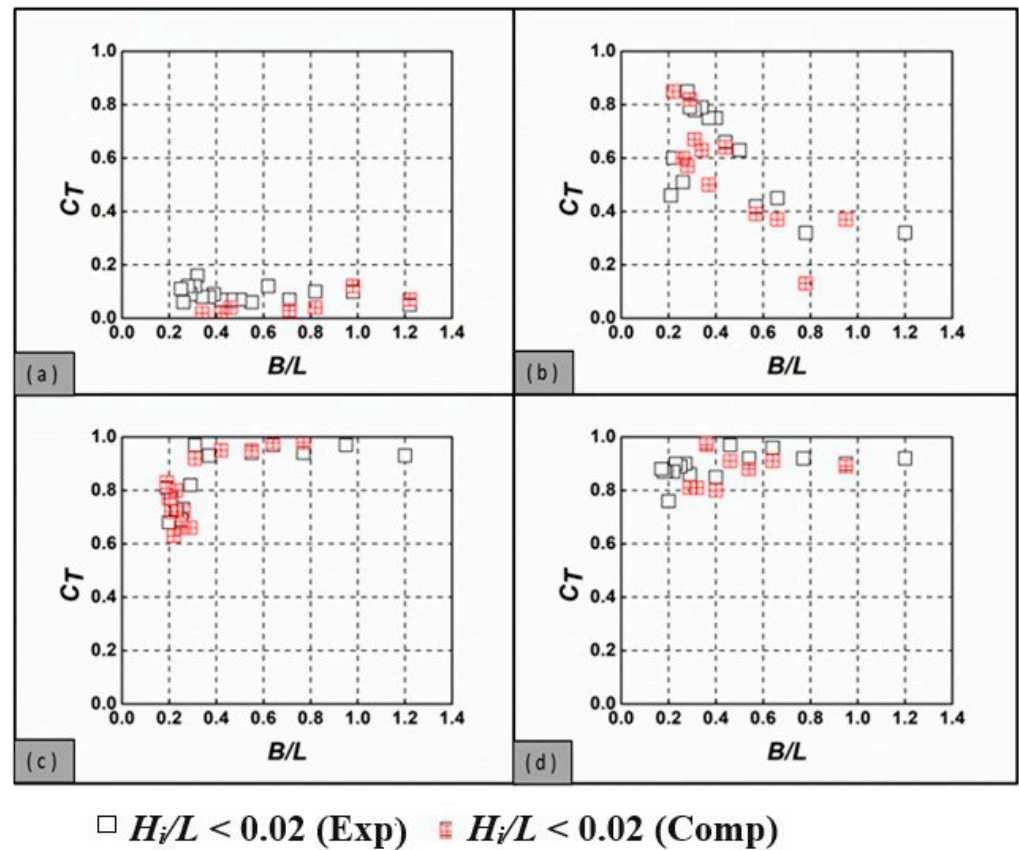


Figure 11. Comparison of experimental and computational C_T at low H_i/L and different d/h ratios: (a) $d/h = 0.667$, (b) $d/h = 1.000$, (c) $d/h = 1.333$, (d) $d/h = 1.667$.

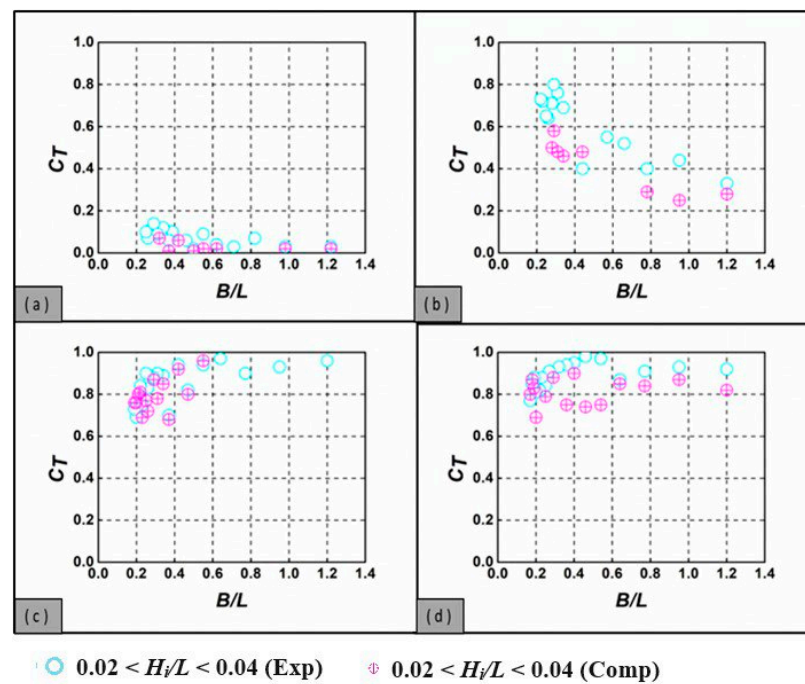


Figure 12. Comparison of experimental and computational C_T at moderate H_i/L and different d/h ratios: (a) $d/h = 0.667$, (b) $d/h = 1.000$, (c) $d/h = 1.333$, (d) $d/h = 1.667$.

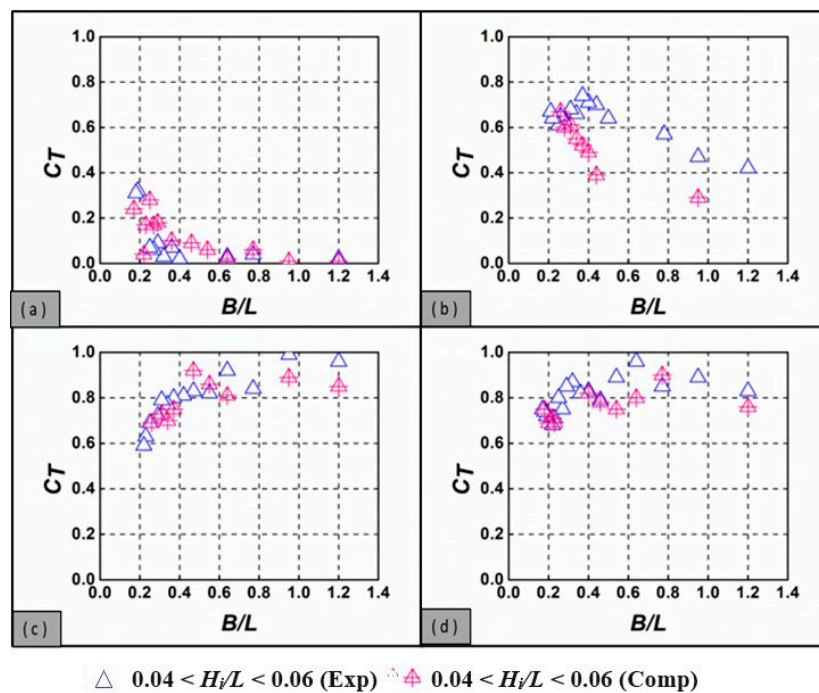


Figure 13. Comparison of experimental and computational C_T at high H_i/L and different d/h ratios: (a) $d/h = 0.667$, (b) $d/h = 1.000$, (c) $d/h = 1.333$, (d) $d/h = 1.667$.

Table 3. Comparative analysis of experimental and computational error deviation data for C_T .

| | | | MSE | RMSE | MAD | MAPE | R^2 |
|------------------------------------|-------------------------------|-----------------------|------|------|------|------|-------|
| Transmission coefficient (C_T) | Emerged SBW ($d/h = 0.667$) | $H_i/L < 0.02$ | 0.00 | 0.04 | 0.04 | 0.49 | 0.88 |
| | | $0.02 < H_i/L < 0.04$ | 0.00 | 0.03 | 0.02 | 0.37 | 0.95 |
| | | $0.04 < H_i/L < 0.06$ | 0.00 | 0.02 | 0.01 | 0.27 | 1.00 |

Table 3. Cont.

| | | MSE | RMSE | MAD | MAPE | R ² | |
|--|---|---------------------------------|------|------|------|----------------|------|
| Transmission coefficient (C _T) | Alternatively submerged SBW (d/h = 1.000) | H _i /L < 0.02 | 0.02 | 0.16 | 0.13 | 0.20 | 0.91 |
| | | 0.02 < H _i /L < 0.04 | 0.04 | 0.19 | 0.17 | 0.29 | 0.79 |
| | | 0.04 < H _i /L < 0.06 | 0.03 | 0.18 | 0.15 | 0.22 | 0.44 |
| | Submerged SBW (d/h = 1.333) | H _i /L < 0.02 | 0.00 | 0.06 | 0.05 | 0.06 | 0.98 |
| | | 0.02 < H _i /L < 0.04 | 0.00 | 0.07 | 0.05 | 0.06 | 0.94 |
| | | 0.04 < H _i /L < 0.06 | 0.00 | 0.06 | 0.04 | 0.06 | 0.93 |
| | Submerged SBW (d/h = 1.667) | H _i /L < 0.02 | 0.00 | 0.03 | 0.03 | 0.04 | 0.99 |
| | | 0.02 < H _i /L < 0.04 | 0.01 | 0.11 | 0.09 | 0.09 | 0.74 |
| | | 0.04 < H _i /L < 0.06 | 0.01 | 0.08 | 0.06 | 0.06 | 0.91 |

4.2. Wave Reflection

The assessment of the SBW’s efficacy in reflecting wave energy is pivotal for gauging its effectiveness in coastal protection. This evaluation centers on the wave reflection coefficient, C_R, which precisely quantifies the ratio of the reflected wave height to the incident wave height. This section delves into both experimental and computational investigations, providing comprehensive insights into the intricate dynamics governing wave reflection by SBW models. By meticulously examining various parameters such as wave steepness (H_i/L), wave period and water depths, these experiments offer valuable insights into the nuanced behavior of the wave reflection coefficient, C_R. The evaluation of the SBW’s capacity to reflect wave energy revolves around the wave reflection coefficient, C_R, which is described as the ratio of the height of the reflected wave (H_R) to the height of the incident wave (H_i) [75,80]. Figure 14 meticulously scrutinizes the wave reflection characteristics of SBW models, examining the impact of H_i/L and d/h ratios. It becomes apparent that the C_R variation in relation to H_i/L is nearly imperceptible for the fully submerged and alternatively submerged SBW when d/h = 1.000, 1.333 and 1.667, indicating its insignificance in this context. In stark contrast, for d/h = 0.667, wave steepness emerges as a significant parameter, with C_R exhibiting an increase as H_i/L decreases. Turning to specific d/h values, the C_R for the emerged SBW (d/h = 0.667) showcases an increase with increasing B/L, featuring relatively high values (ranging from 0.46 to 0.95) compared to d/h = 1.000 and 1.333. Concurrently, C_T values exhibit an increase with increasing H_i/L for d/h = 0.667. The influence of B/L on C_R is particularly noteworthy, especially at B/L less than 0.4, with a sharp C_R decline observed for alternatively and fully submerged SBW, reaching a minimum at 0.3 < B/L < 0.5. Subsequently, C_R exhibits a small peak at B/L = 0.4 before gradually declining for the larger B/L range, showcasing intriguing behavior consistent for d/h = 1.000, 1.333 and 1.667. The bragging effect of C_R, reported in large-scale SBWs [81,82], underscores the complexity of the relationship. In summary, the proposed SBW demonstrates high reflectivity (0 < C_R < 0.7) against longer waves (B/L < 0.3) for d/h = 1.000, 1.333 and 1.667). A comparison of C_R graphs in Figure 14a–d suggests that wave reflection by the emerged SBW is more dominant than the alternatively submerged SBW, likely due to its greater disruption of incident waves. This is likely due to the greater disruption of incident waves by the emerged structure. Similar findings from studies on submerged SBWs and rectangular breakwaters support this observation, showing that greater submersion results in less wave reflection [79]. The pronounced wave reflection characteristics of the SBW within the lower B/L range in Figure 14b–d result in diminished wave transmission, as illustrated in Figure 10. Ultimately, the proposed SBW emerges as a robust reflector for d/h = 0.667 for all B/L values and only for B/L less than 0.3 for d/h = 1.000–1.667, with an improvement of approximately 10% to 20%, the alternatively submerged SBW outperforms the submerged SBW in terms of reflective performance.

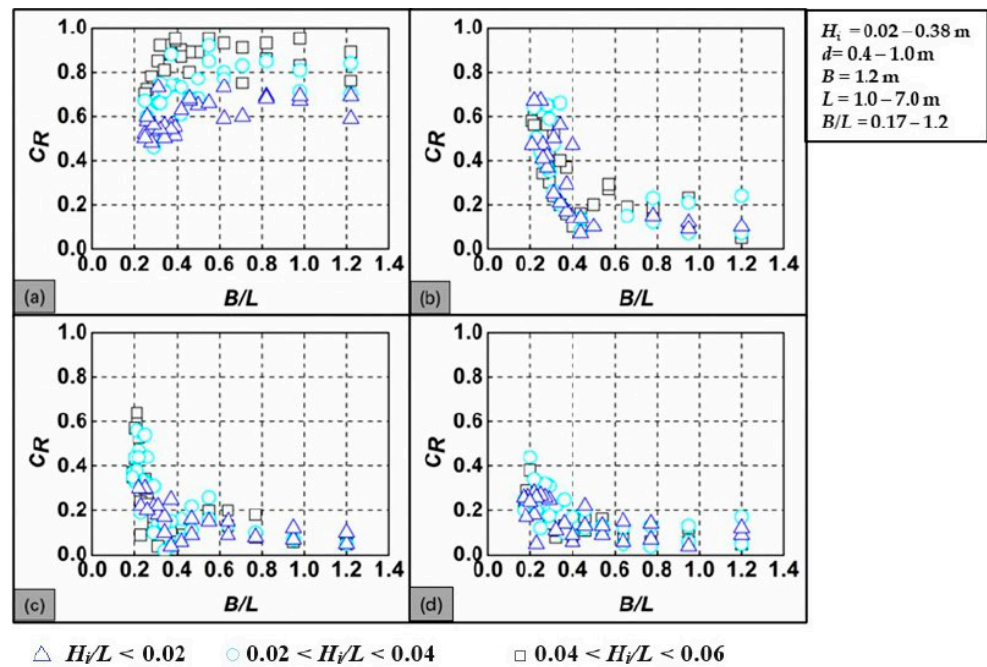


Figure 14. C_R of SBW—(a) $d/h = 0.667$, (b) $d/h = 1.000$, (c) $d/h = 1.333$, (d) $d/h = 1.667$.

The experimental validation of C_R using computational analysis is presented, comparing across different H_i/L and various d/h ratios. Figures 15–17 illustrate this comparison at low, moderate and high wave steepnesses, respectively, showing consistency across d/h ratios. Results from both analyses demonstrate remarkable consistency, affirming the reliability and accuracy of the computational approach in predicting reflection coefficients. Additionally, Table 4 offers a detailed comparison of error deviation data for the C_R between experimental and computational results across all H_i/L and d/h ratios. The computational model consistently shows effective predictive capabilities, with error analyses like MSE , MAD , $MAPE$ and R^2 affirming its accuracy in capturing the reflective properties of SBW models across diverse conditions.

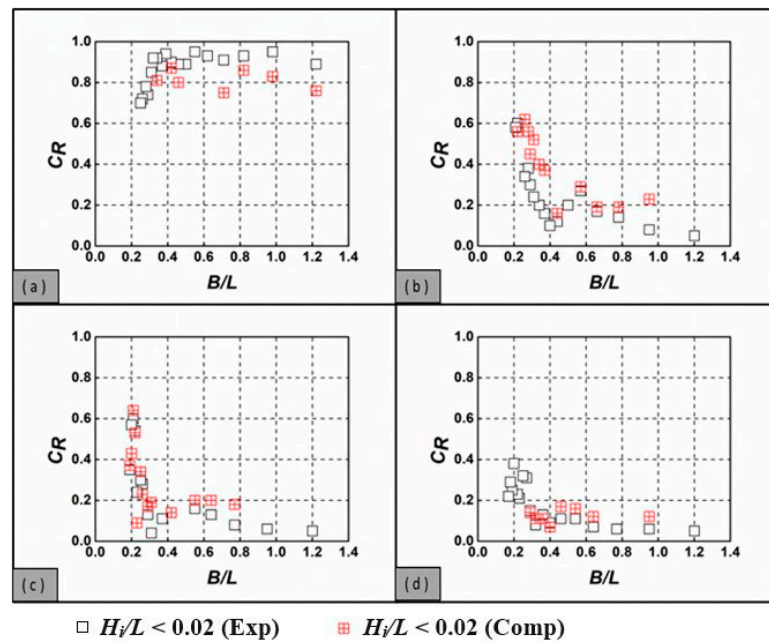


Figure 15. Comparison of experimental and computational C_R at low H_i/L and different d/h ratios: (a) $d/h = 0.667$, (b) $d/h = 1.000$, (c) $d/h = 1.333$, (d) $d/h = 1.667$.

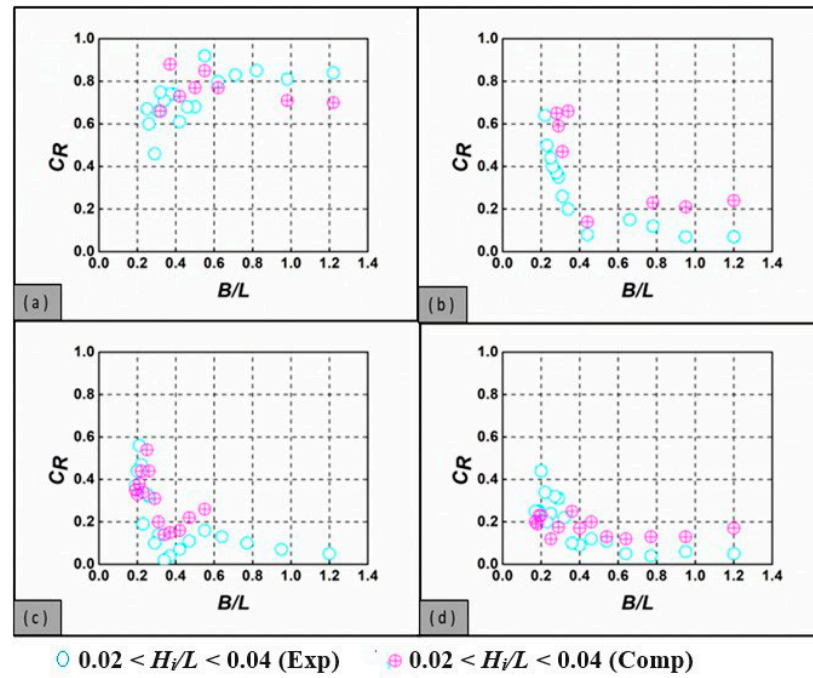


Figure 16. Comparison of experimental and computational C_R at moderate H_i/L and different d/h ratios: (a) $d/h = 0.667$, (b) $d/h = 1.000$, (c) $d/h = 1.333$, (d) $d/h = 1.667$.

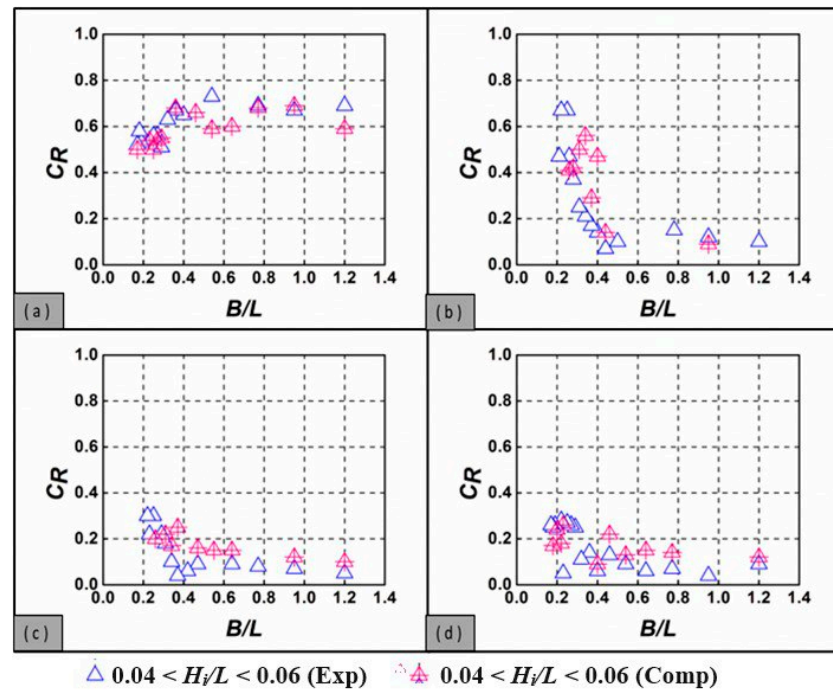


Figure 17. Comparison of experimental and computational C_R at high H_i/L and different d/h ratios: (a) $d/h = 0.667$, (b) $d/h = 1.000$, (c) $d/h = 1.333$, (d) $d/h = 1.667$.

Table 4. Comparative analysis of experimental and computational error deviation data for C_R .

| | | | MSE | RMSE | MAD | MAPE | R^2 |
|----------------------------------|-------------------------------|-----------------------|------|------|------|------|-------|
| Reflection coefficient (C_R) | Emerged SBW ($d/h = 0.667$) | $H_i/L < 0.02$ | 0.01 | 0.11 | 0.10 | 0.11 | 0.30 |
| | | $0.02 < H_i/L < 0.04$ | 0.01 | 0.10 | 0.10 | 0.13 | 0.86 |
| | | $0.04 < H_i/L < 0.06$ | 0.00 | 0.06 | 0.04 | 0.06 | 0.95 |

Table 4. Cont.

| | | MSE | RMSE | MAD | MAPE | R ² | |
|--|---|---------------------------------|------|------|------|----------------|------|
| Reflection coefficient (C _R) | Alternatively submerged SBW (d/h = 1.000) | H _i /L < 0.02 | 0.03 | 0.17 | 0.15 | 0.46 | 0.71 |
| | | 0.02 < H _i /L < 0.04 | 0.06 | 0.24 | 0.21 | 0.58 | 0.44 |
| | | 0.04 < H _i /L < 0.06 | 0.04 | 0.20 | 0.16 | 0.41 | 0.61 |
| | Submerged SBW (d/h = 1.333) | H _i /L < 0.02 | 0.01 | 0.09 | 0.07 | 0.61 | 0.95 |
| | | 0.02 < H _i /L < 0.04 | 0.01 | 0.12 | 0.11 | 0.53 | 0.89 |
| | | 0.04 < H _i /L < 0.06 | 0.00 | 0.05 | 0.04 | 0.50 | 0.80 |
| | Submerged SBW (d/h = 1.667) | H _i /L < 0.02 | 0.00 | 0.04 | 0.04 | 0.44 | 0.95 |
| | | 0.02 < H _i /L < 0.04 | 0.01 | 0.1 | 0.09 | 0.88 | 0.9 |
| | | 0.04 < H _i /L < 0.06 | 0.01 | 0.08 | 0.06 | 0.06 | 0.91 |

4.3. Wave Energy Loss

The examination of wave energy loss associated with SBW models constitutes a critical aspect of understanding their efficacy as coastal protection measures. This analysis provides a detailed exploration of both experimental and computational wave energy loss, experimental validation of energy loss coefficients using computational analysis, and error analysis for wave energy loss. By synthesizing insights from these analyses, a comprehensive understanding of the factors influencing wave energy dissipation and the effectiveness of SBWs in mitigating coastal hazards is provided. The effectiveness of the SBW is gauged by its wave reflection, transmission and energy dissipation attributes [5]. The wave dissipation coefficient, C_L, serves as an indicator of hydraulic efficiency, derived from the energy conservation law (C_T² + C_R² + C_L² = 1) [71,75,82–85].

The efficacy of SBW in mitigating wave energy is pivotal for assessing their viability as coastal defence solutions. SBWs, distinguished by their curvature, exhibit notably higher energy dissipation compared to conventional types [86]. Figure 18 elucidates the variation of C_L across SBWs with different B/L and H_i/L under regular wave conditions. Notably, emerged and fully submerged SBWs generally display lower wave energy attenuation compared to alternatively submerged SBWs, a phenomenon attributed to the pronounced curvature, particularly prominent for d/h = 1.000. Interestingly, the alternatively submerged SBW with d/h = 1.000 effectively intercepts incoming waves, leading to enhanced energy dissipation as waves traverse the crest. Figure 18b underscores this effect, showcasing a significant increase in C_L with B/L, especially for shorter wavelengths, highlighting efficient energy release upon wave impact. Conversely, for d/h = 0.667, 1.333 and 1.667, C_L decreases with increasing B/L, demonstrating varied behavior dependent on relative water depth. The influence of H_i/L on C_L varies across different d/h and B/L values, with distinct trends observed for d/h = 0.667, 1.333 and 1.667, primarily driven by wave breaking over the SBW. In summary, the alternatively submerged SBW (d/h = 1.000) exhibits superior wave dissipation performance compared to fully submerged SBWs (d/h = 1.667 and 1.333), with emerged SBWs at d/h = 0.667 showing similar efficacy. In fully submerged breakwaters, similar findings from studies on SBWs and rectangular breakwaters indicate that higher submergence leads to a lower dissipation coefficient. Conversely, less submerged breakwaters cause the dissipation coefficient to rise, reflecting increased wave interaction and energy dissipation [79].

Figures 19–21 provide a comparison between experimental and computational C_L values across different H_i/L categories and various d/h ratios (d/h = 0.667, d/h = 1.000, d/h = 1.333 and d/h = 1.667). These figures offer a comprehensive examination of C_L under varying wave conditions. The comparison between experimental and computational results within each figure category enables a thorough assessment of the computational model’s accuracy. Remarkably consistent results between experimental and computational analyses are observed, indicating the reliability and precision of the computational approach in

predicting energy loss coefficients. Additionally, Table 5 offers a detailed comparison of error deviation data for C_L between experimental and computational results across all H_i/L and d/h ratios. The computational model consistently demonstrates a robust fit with experimental outcomes, showcasing effective predictive capabilities across various H_i/L and d/h ratios. Metrics such as Mean Squared Error (MSE), Root Mean Squared Error (RMSE), Mean Absolute Deviation (MAD), Mean Absolute Percentage Error (MAPE) and R-squared (R^2) values affirm the accuracy of the model in capturing the energy dissipation properties of SBW models across the entire spectrum of H_i/L and d/h ratios.

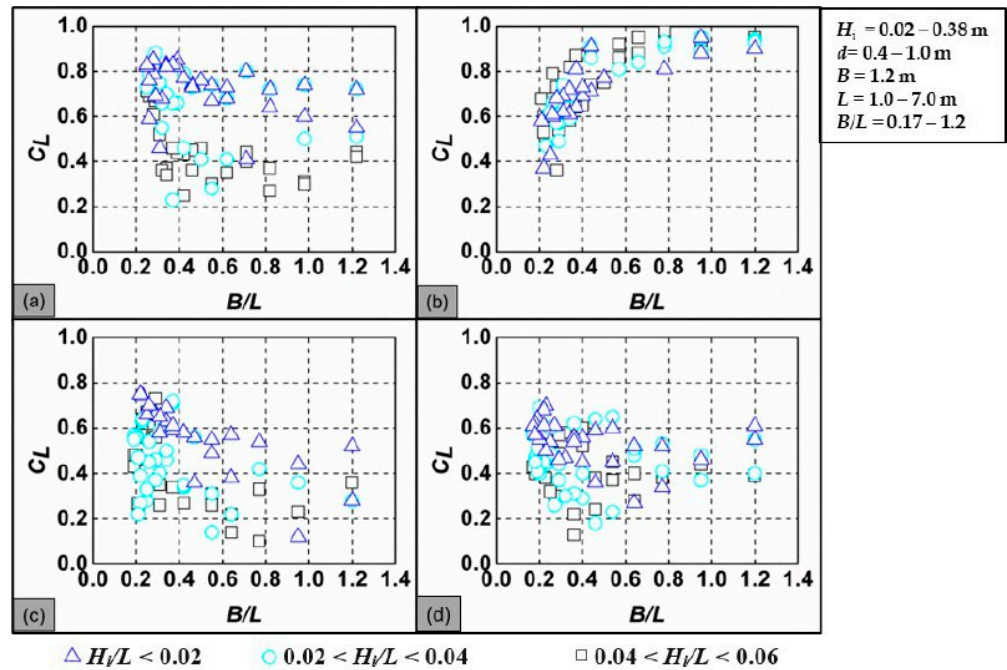


Figure 18. C_L of SBW—(a) $d/h = 0.667$, (b) $d/h = 1.000$, (c) $d/h = 1.333$, (d) $d/h = 1.667$.

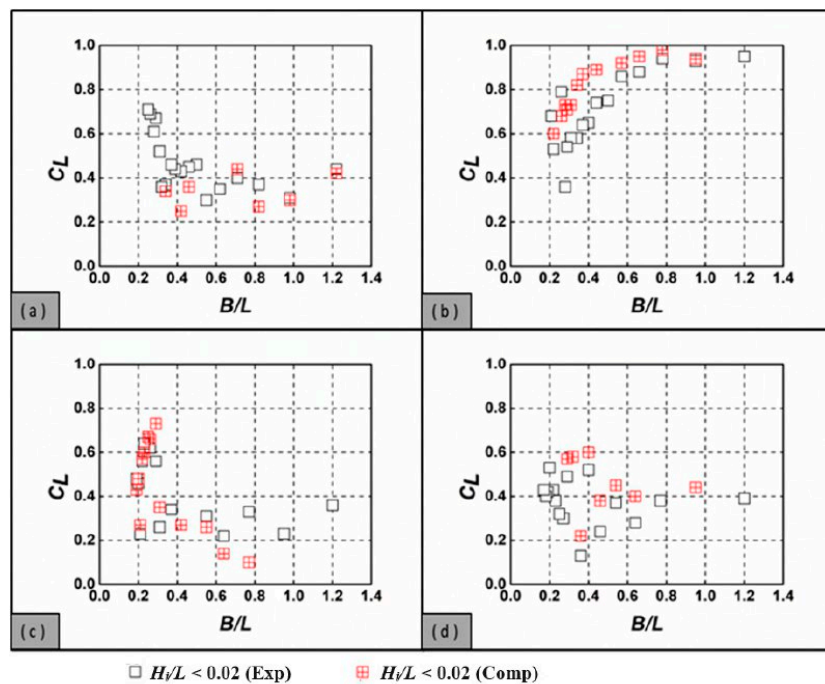


Figure 19. Comparison of experimental and computational C_L at low wave H_i/L and different d/h ratios: (a) $d/h = 0.667$, (b) $d/h = 1.000$, (c) $d/h = 1.333$, (d) $d/h = 1.667$.

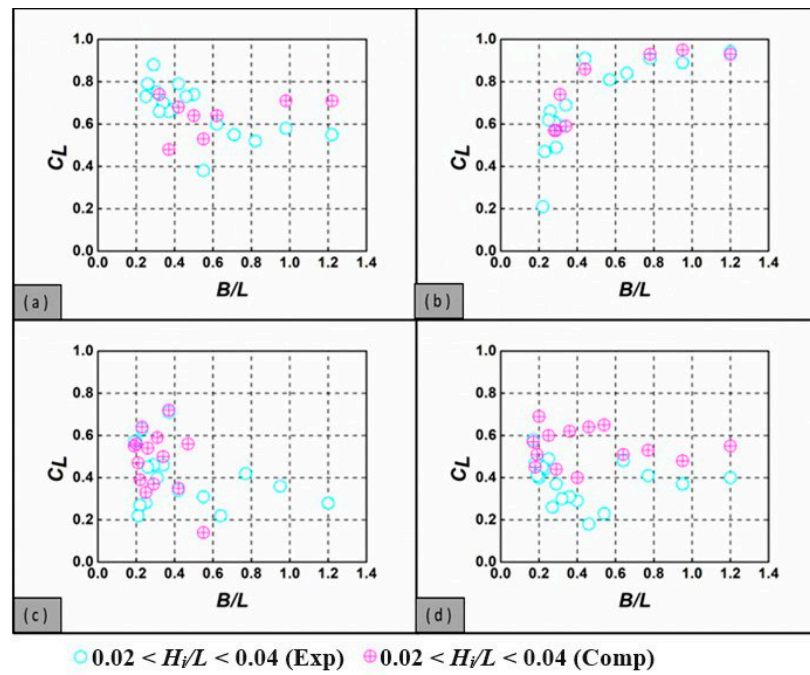


Figure 20. Comparison of experimental and computational C_L at moderate H_i/L and different d/h ratios: (a) $d/h = 0.667$, (b) $d/h = 1.000$, (c) $d/h = 1.333$, (d) $d/h = 1.667$.

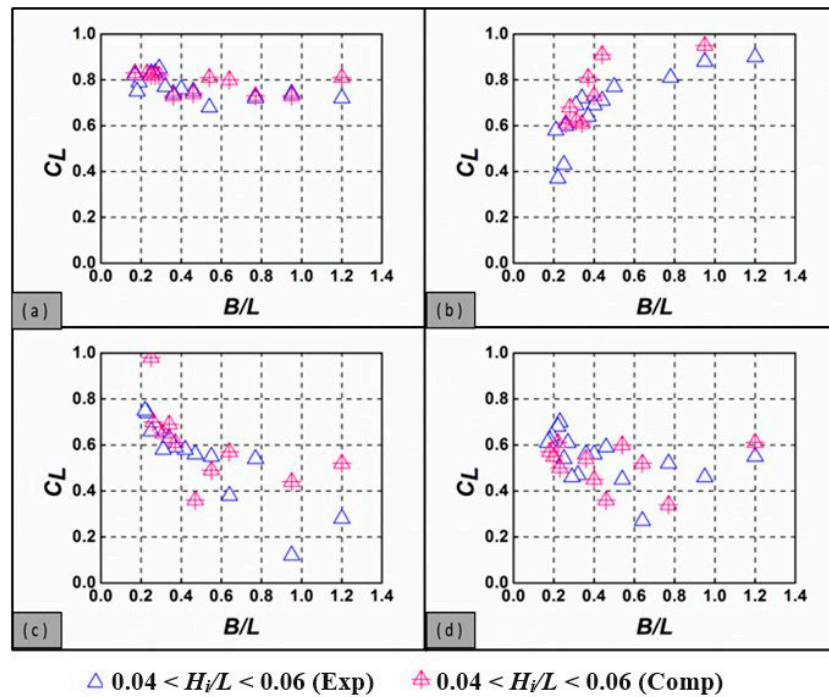


Figure 21. Comparison of experimental and computational C_L at high H_i/L and different d/h ratios: (a) $d/h = 0.667$, (b) $d/h = 1.000$, (c) $d/h = 1.333$, (d) $d/h = 1.667$.

Table 5. Comparative analysis of experimental and computational error deviation data for C_L .

| | | MSE | $RMSE$ | MAD | $MAPE$ | R^2 |
|-----------------------------------|-------------------------------|-----------------------|--------|-------|--------|-------|
| Energy loss coefficient (C_L) | Emerged SBW ($d/h = 0.667$) | $H_i/L < 0.02$ | 0.01 | 0.09 | 0.07 | 0.80 |
| | | $0.02 < H_i/L < 0.04$ | 0.02 | 0.13 | 0.12 | 0.82 |
| | | $0.04 < H_i/L < 0.06$ | 0.00 | 0.05 | 0.03 | 0.95 |

Table 5. Cont.

| | | MSE | RMSE | MAD | MAPE | R ² | |
|-----------------------------------|---|-----------------------|------|------|------|----------------|------|
| Energy loss coefficient (C_L) | Alternatively submerged SBW ($d/h = 1.000$) | $H_i/L < 0.02$ | 0.02 | 0.14 | 0.10 | 0.18 | 0.93 |
| | | $0.02 < H_i/L < 0.04$ | 0.01 | 0.07 | 0.06 | 0.09 | 0.96 |
| | | $0.04 < H_i/L < 0.06$ | 0.01 | 0.11 | 0.09 | 0.12 | 0.77 |
| | Submerged SBW ($d/h = 1.333$) | $H_i/L < 0.02$ | 0.01 | 0.09 | 0.07 | 0.20 | 0.94 |
| | | $0.02 < H_i/L < 0.04$ | 0.01 | 0.11 | 0.08 | 0.24 | 0.90 |
| | | $0.04 < H_i/L < 0.06$ | 0.02 | 0.15 | 0.10 | 0.42 | 0.82 |
| | Submerged SBW $d/h = 1.667$ | $H_i/L < 0.02$ | 0.01 | 0.09 | 0.07 | 0.27 | 0.96 |
| | | $0.02 < H_i/L < 0.04$ | 0.05 | 0.22 | 0.16 | 0.59 | 0.42 |
| | | $0.04 < H_i/L < 0.06$ | 0.02 | 0.15 | 0.12 | 0.25 | 0.71 |

4.4. Wave Forces on SBW

Figure 22a–d provide a visual representation of the temporal evolution of pressure contour plots at a specific time ($t = 30.6$ s) for SBW with different d/h ratios ($d/h = 0.667, 1.000, 1.333, 1.667$) under the influence of waves with a period of 1.6 s and H_i/L of 0.02. The contours depict the pressure distribution on the surface of the SBW, revealing that an increase in d/h results in a proportional escalation of pressure magnitude. This observation infers that larger waves exert more significant forces on the SBW. Notably, the pressure levels at the SBW’s surface are comparatively lower than those encountered at greater depths, suggesting a gradual rise in pressure from the surface towards the depths of the SBW. This phenomenon is attributed to the additional hydrostatic pressure exerted by the water column above the SBWs surface.

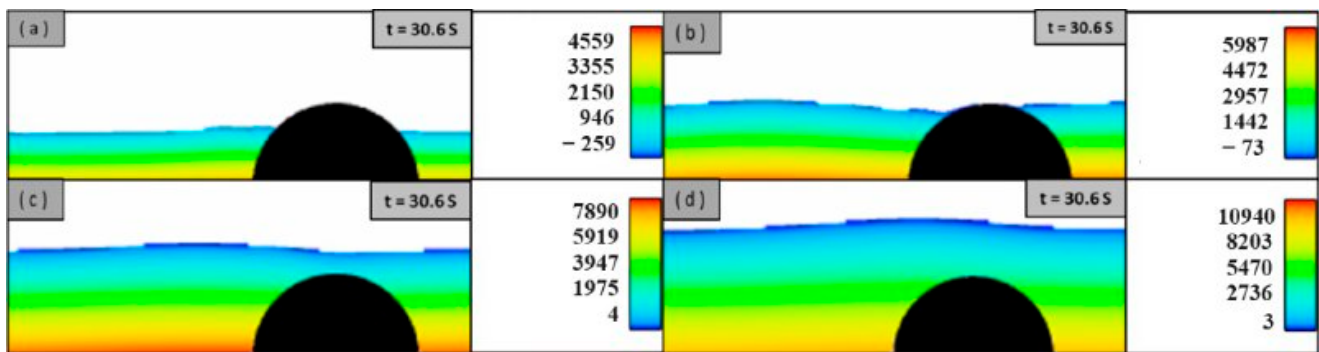


Figure 22. Temporal evolution of pressure (Pa) contour at $t = 30.6$ s—(a) $d/h = 0.667$, (b) $d/h = 1.000$, (c) $d/h = 1.333$, (d) $d/h = 1.667$.

In Figures 23 and 24, the temporal evolution of horizontal (F_h) and vertical force (F_v) variations on the SBW is depicted under different d/h ratios ($d/h = 0.667, d/h = 1.000, d/h = 1.333, d/h = 1.667$). Figure 23 illustrates that F_h consistently fall within the specified range of -200 N to +200 N for all four cases on the interval from 20 to 40 s, providing a detailed examination of the SBW’s horizontal forces. Simultaneously, Figure 24 presents the evolution of F_v , showcasing distinct ranges for each d/h ratio. For instance, F_v for $d/h = 0.667$ (Figure 24b) range from 360 N to 480 N, while for $d/h = 1.000$ (Figure 24c), the F_v vary from 660 N to 800 N, illustrating the dynamic forces exerted on the SBW as influenced by wave conditions and water depth. When $d/h = 1.333$ (Figure 24d), F_v exhibit a range of 680 N to 880 N, further emphasizing the influence of water depth on the forces exerted. For $d/h = 1.667$ (Figure 24d), F_v exhibit a range of 699 N to 791 N. These outcomes utilize a wave period of 1.6 s and H_i/L of 0.02.

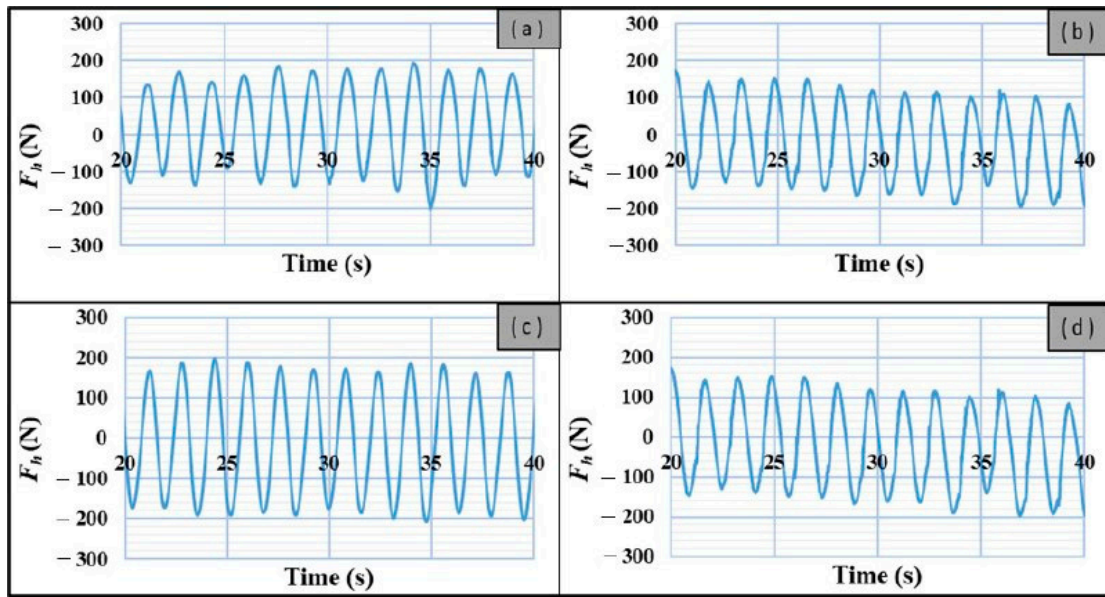


Figure 23. Temporal evolution of F_h variation (a) $d/h = 0.667$, (b) $d/h = 1.000$, (c) $d/h = 1.333$, (d) $d/h = 1.667$.

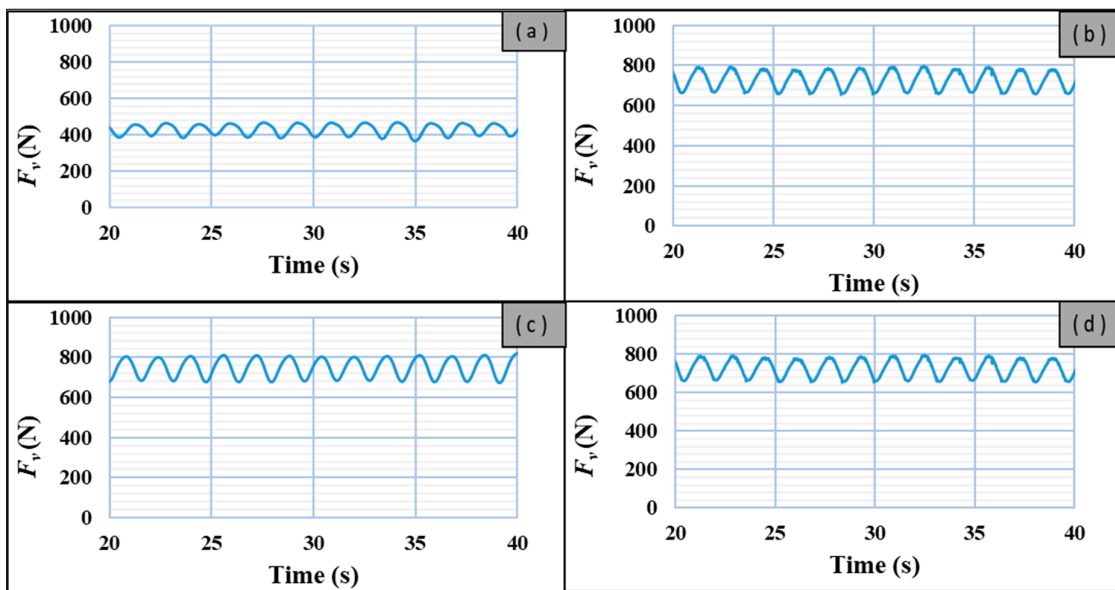


Figure 24. Temporal evolution of F_v variation (a) $d/h = 0.667$, (b) $d/h = 1.000$, (c) $d/h = 1.333$, (d) $d/h = 1.667$.

4.4.1. Horizontal Force Analysis on SBW

Figures 25 and 26 offer the analysis of average horizontal peak force due to wave trough ($F_{h,t}$) and average horizontal peak force due to wave crest ($F_{h,c}$) concerning $d/h = 0.667$, $d/h = 1.000$, $d/h = 1.333$ and $d/h = 1.667$ conditions, spanning three H_i/L ranges ($H_i/L < 0.02$, $0.02 < H_i/L < 0.04$, $0.04 < H_i/L < 0.06$). Examination of $F_{h,t}$ in Figure 25 and $F_{h,c}$ in Figure 26 reveals an inverse correlation with B/L values, indicating that as B/L increases, $F_{h,t}$ and $F_{h,c}$ tend to decrease. In emerged cases, $d/h = 0.667$ in Figures 25a and 26a, higher H_i/L increases $F_{h,t}$ and $F_{h,c}$ due to concentrated energy, while $F_{h,c}$ decreases because of steeper shapes. Despite this, $F_{h,c}$ remains dominant due to its greater momentum. Conversely, in Figure 25b–d, decreasing H_i/L increases $F_{h,t}$ and $F_{h,c}$, driven by broader crests and shallower troughs concentrating more energy, alongside improved C_T through the SBW. Figure 25 depicts scenarios for $d/h = 0.667$, $d/h = 1.000$, $d/h = 1.333$ and $d/h = 1.667$,

showing dynamic interactions for $F_{h,t}$ (ranging from 4 to 194 for $d/h = 0.667$, 2 to 454 for $d/h = 1.000$, 16 to 308 for $d/h = 1.333$ and 14.3 to 432.2 for $d/h = 1.667$), indicating the complex interplay of forces. Figure 26 illustrates $F_{h,c}$ for $d/h = 0.667$, $d/h = 1.000$, $d/h = 1.333$ and $d/h = 1.667$ conditions, revealing distinct relationships with B/L and H_i/L . The observed ranges (ranging from 30 to 292 for $d/h = 0.667$, 16 to 500 for $d/h = 1.000$, 4 to 432 for $d/h = 1.333$ and 0.6 to 371 for $d/h = 1.667$) signify varying magnitudes of forces due to wave crests, attributed to the dynamic interplay between wave characteristics and water depth.

4.4.2. Vertical Force Analysis on SBW

In the vertical force analysis of the SBW, Figures 27 and 28 provide the vertical peak force due to the wave trough ($F_{v,t}$) and the average vertical peak force due to the wave crest ($F_{v,c}$), respectively. The study encompasses various H_i/L ranges ($H_i/L < 0.02$, $0.02 < H_i/L < 0.04$, $0.04 < H_i/L < 0.06$) across different d/h conditions (0.667, 1.000, 1.333 and 1.667). In the emerged SBW (Figure 27a— $d/h = 0.667$), $F_{v,t}$ ranges from 400 to 426, while for $d/h = 1.000$ (Figure 27b), $d/h = 1.333$ (Figure 27c) and $d/h = 1.667$ (Figure 27d) conditions, the ranges are 660 to 736, 648 to 772 and 702.2 to 755.2, respectively. These fluctuations highlight the influence of water depth on interaction dynamics, as increased B/L leads to reduced peak forces. In the emerged SBW (Figure 28a— $d/h = 0.667$), $F_{v,c}$ varies from 430 to 578. For alternatively submerged SBW (Figure 28b— $d/h = 1.000$) conditions, it ranges from 742 to 822, and for fully submerged SBW (Figure 28c— $d/h = 1.333$, Figure 28d— $d/h = 1.667$) scenarios, it ranges from 742 to 822 and from 744.4 to 840.8, respectively. While the effect of H_i/L on these forces is less pronounced, indicating a relatively limited impact on the vertical forces acting on the SBW.

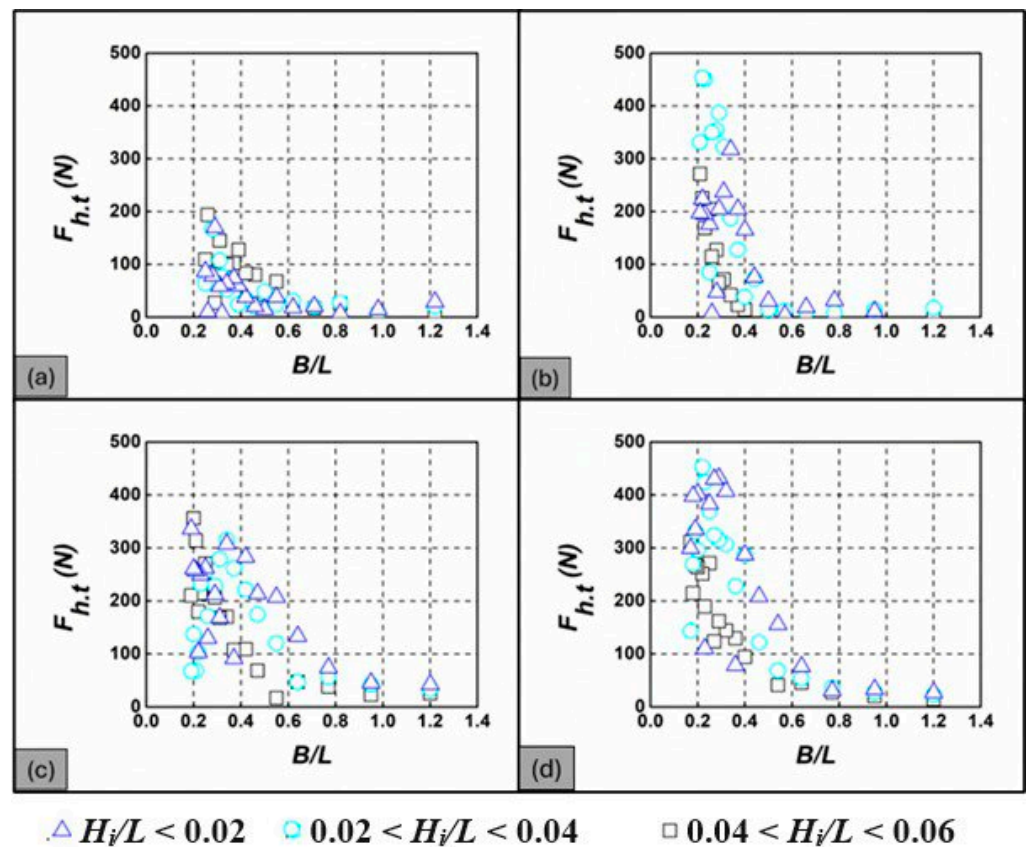


Figure 25. Average horizontal peak force due to wave trough ($F_{h,t}$)—(a) $d/h = 0.667$, (b) $d/h = 1.000$, (c) $d/h = 1.333$, (d) $d/h = 1.667$.

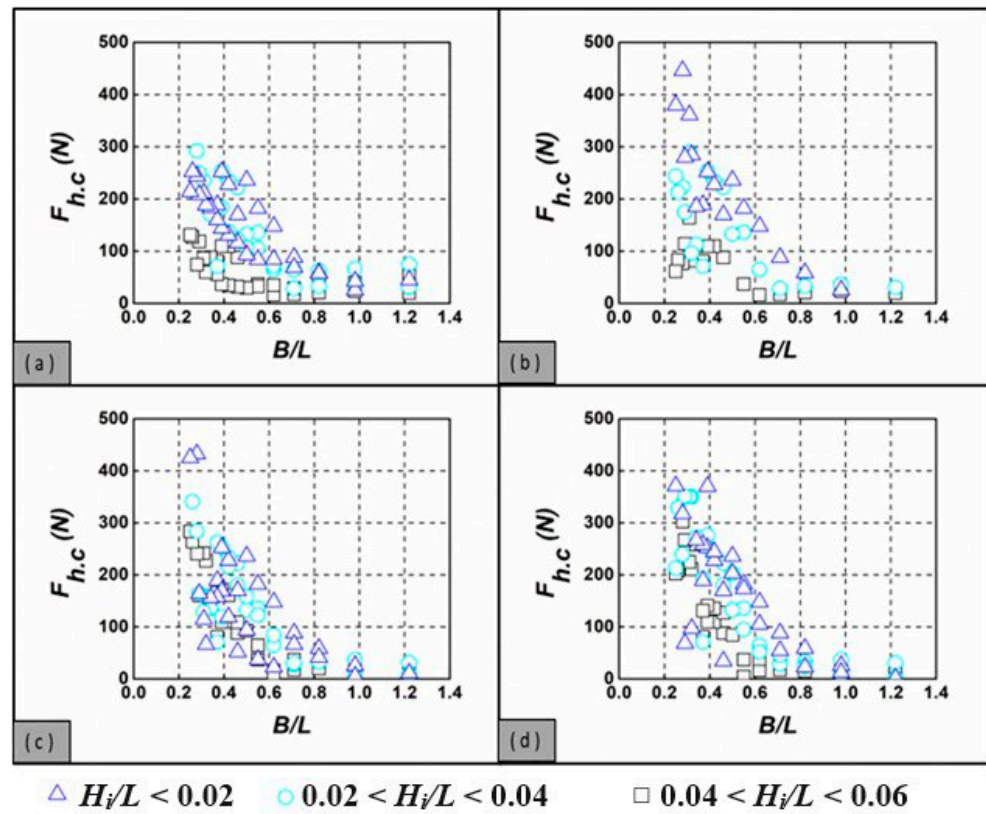


Figure 26. Average horizontal peak force due to wave crest ($F_{h,c}$)—(a) $d/h = 0.667$, (b) $d/h = 1.000$, (c) $d/h = 1.333$, (d) $d/h = 1.667$.

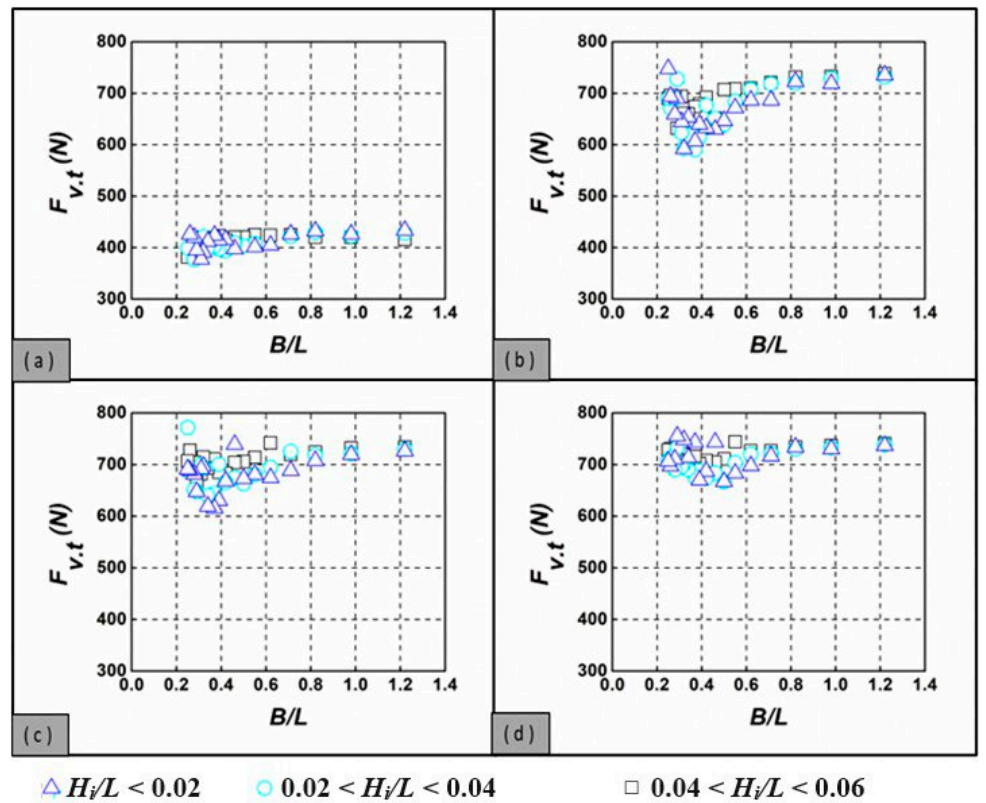


Figure 27. Average vertical peak force due to wave trough ($F_{v,t}$)—(a) $d/h = 0.667$, (b) $d/h = 1.000$, (c) $d/h = 1.333$, (d) $d/h = 1.667$.

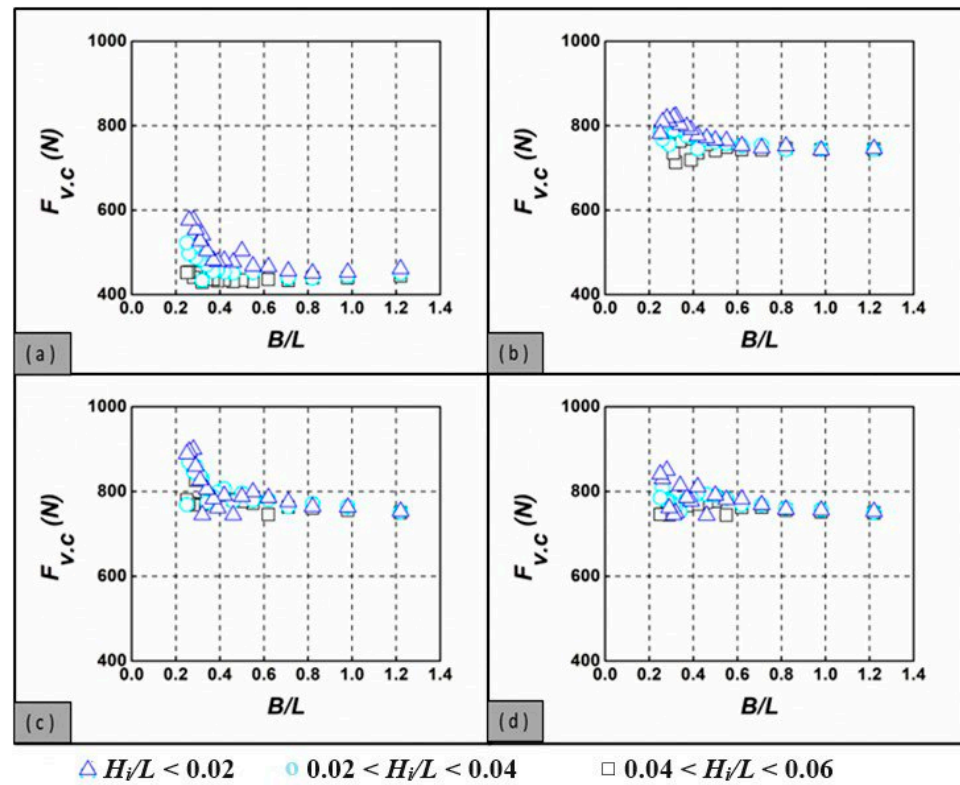


Figure 28. Average vertical peak force due to wave crest ($F_{v,c}$)—(a) $d/h = 0.667$, (b) $d/h = 1.000$, (c) $d/h = 1.333$, (d) $d/h = 1.667$.

5. Conclusions

This study presents the development and evaluation of small SBW designed for diverse coastal protection applications. The hydraulic characteristics of the proposed SBW were investigated through a combined approach involving physical and computational modelling. Notably, the analysis of the C_T revealed nuanced effectiveness across SBW, with the emerged SBW ($d/h = 0.667$) exhibiting a smaller C_T compared to $d/h = 1.000$, $d/h = 1.333$ and 1.667 . Crucially by correlating C_T values with B/L ratios and comparing the transmitted wave height with the permissible wave height criteria for mangrove sampling survival, the success of the SBW at different B/L dimensions have been assessed. The SBW demonstrates a reflection accuracy of nearly 95% when d/h equals 0.667. The alternatively submerged SBW ($d/h = 1.000$) demonstrated superior wave attenuation performance, surpassing the fully submerged SBW ($d/h = 1.667$) and achieving a substantial 70% reduction in incident wave height when exposed to regular waves with shorter periods. Moreover, the SBW with ($d/h = 1.000$) displayed higher wave reflection, approximately 10% more than the fully submerged SBW when facing longer period waves. This reflection occurred notably at B/L less than 0.4 for $d/h = 1.000$ – 1.667 . The SBW, when alternatively submerged SBW and subjected to shorter waves, showcased superior energy dissipation performance, reaching up to 90% wave energy dissipation. However, it is crucial to acknowledge that wave energy dissipation tended to deteriorate as the immersion depth increased. Computational results aligned well with experimental findings, demonstrating the computational model’s success in simulating free surface flows in coastal engineering. Analyzing horizontal forces in the SBW, the average horizontal peak force due to wave crest ($F_{h,c}$) displayed variations across scenarios, with $F_{h,c}$ being higher on submerged SBW compared to emerged SBW. Vertical forces in the SBW showed that $F_{v,t}$ was lower in the emerged condition than in alternative and full submersion, indicating increased forces during wave troughs with deeper immersion. $F_{v,c}$ was higher during wave crests in the emerged condition and for alternative and full submersion, with limited impact of H_i/L on forces.

Author Contributions: F.A.H.A.-T.: Conceptualization, Data curation, Formal analysis, Resources, Visualization, Writing—original draft; H.-M.T.: Supervision, Resources, Conceptualization, Project administration, original draft, Writing—review and editing; Z.M.: Review; I.A.J.: Review; A.S.: Review; E.H.H.A.-Q.: Data curation. All authors have read and agreed to the published version of the manuscript.

Funding: YUTP-FRG (015LC0-352) and Ministry of Higher Education Malaysia (FRGS/1/2018/TK10/UTP/02/8).

Institutional Review Board Statement: Not applicable.

Informed Consent Statement: Not applicable.

Data Availability Statement: The data that support the findings of this study are available on request from the corresponding authors.

Acknowledgments: Special appreciation to Yayasan Universiti Teknologi PETRONAS (YUTP) and Ministry of Higher Education Malaysia (MOHE) for funding the research through grants 015LC0-352 and FRGS/1/2018/TK10/UTP/02/8, respectively.

Conflicts of Interest: The authors declare no conflicts of interest.

References

1. Wang, H.; Foltz, W.; Zhang, N.; Dermisis, D. Numerical and Experimental Analyses of Breakwater Designs for Turbulent Flow Characteristics and Sediment Transport under Coastal Wave Actions. *J. Fluids Eng.* **2020**, *142*, 071207. [[CrossRef](#)]
2. Schoonees, T.; Gijón Mancheño, A.; Scheres, B.; Bouma, T.J.; Silva, R.; Schlurmann, T.; Schüttrumpf, H. Hard structures for coastal protection, towards greener designs. *Estuaries Coasts* **2019**, *42*, 1709–1729. [[CrossRef](#)]
3. Takahashi, S. *Design of Vertical Breakwaters*; Reference Document; Citeseer, Port and Harbor Research Institute: Yokosuka, Japan, 2002; Volume 34, 106p.
4. Shukla, J.; Rajwani, L.; Shah, D. Analysis and Design of Breakwater for Sea Water Intake Facility on South East Coast of India. In Proceedings of the International Conference on Case Histories in Geotechnical Engineering, Chicago, IL, USA, 25–28 September 2013.
5. Romya, A.A.; Moghazy, H.M.; Iskander, M.M.; Abdelrazek, A.M. Performance assessment of corrugated semi-circular breakwaters for coastal protection. *Alex. Eng. J.* **2022**, *61*, 3587–3598. [[CrossRef](#)]
6. Gomaa, M.A.; Kasem, T.H.; Huzayyin, O.A.; Schlenkhoff, A.; Sasaki, J. Numerical Simulation and Piv Measurements of the Wave-Induced Flow Field Near Semi-Circular Breakwaters. *SN Appl. Sci.* **2023**, *175*, 7. [[CrossRef](#)]
7. Gomes, A.; Pinho, J.L.S.; Valente, T.; Antunes do Carmo, J.S.; Hegde, A.V. Performance assessment of a semi-circular breakwater through CFD modelling. *J. Mar. Sci. Eng.* **2020**, *8*, 226. [[CrossRef](#)]
8. Al-Towayti, F.A.H.; Min, T.H. Performance Characteristics of a Submerged Semicircular Breakwater Exposed to Regular Waves: An Experimental Study. In *E3S Web of Conferences*; EDP Sciences: Les Ulis, France, 2024.
9. Hunt, I.A., Jr. Design of seawalls and breakwaters. *J. Waterw. Harb. Div.* **1959**, *85*, 123–152. [[CrossRef](#)]
10. Burcharth, H.F. The design of breakwaters. In *Coastal, Estuarial and Harbour Engineers' Reference Book*; Spon Press: London, UK, 1994; pp. 381–424.
11. Srikanth, S.; Lum, S.K.Y.; Chen, Z.J.T. Mangrove root: Adaptations and ecological importance. *Trees* **2016**, *30*, 451–465. [[CrossRef](#)]
12. Friess, D.A.; Rogers, K.; Lovelock, C.E.; Krauss, K.W.; Hamilton, S.E.; Lee, S.Y.; Lucas, R.; Primavera, J.; Rajkaran, A.; Shi, S. The state of the world's mangrove forests: Past, present, and future. *Annu. Rev. Environ. Resour.* **2019**, *44*, 89–115. [[CrossRef](#)]
13. Hamilton, S.E.; Casey, D. Creation of a high spatio-temporal resolution global database of continuous mangrove forest cover for the 21st century (CGMFC-21). *Glob. Ecol. Biogeogr.* **2016**, *25*, 729–738. [[CrossRef](#)]
14. Alongi, D.M. Carbon sequestration in mangrove forests. *Carbon Manag.* **2012**, *3*, 313–322. [[CrossRef](#)]
15. Primavera, J.H. Development and conservation of Philippine mangroves: Institutional issues. *Ecol. Econ.* **2000**, *35*, 91–106. [[CrossRef](#)]
16. Lee, S.Y.; Hamilton, S.; Barbier, E.B.; Primavera, J.; Lewis, R.R., III. Better restoration policies are needed to conserve mangrove ecosystems. *Nat. Ecol. Evol.* **2019**, *3*, 870–872. [[CrossRef](#)] [[PubMed](#)]
17. Primavera, J.H.; Esteban, J.M.A. A review of mangrove rehabilitation in the Philippines: Successes, failures and future prospects. *Wetl. Ecol. Manag.* **2008**, *16*, 345–358. [[CrossRef](#)]
18. Thompson, B.S. The political ecology of mangrove forest restoration in Thailand: Institutional arrangements and power dynamics. *Land Use Policy* **2018**, *78*, 503–514. [[CrossRef](#)]
19. Xue, S.; Xu, Y.; Xu, G.; Wang, J.; Chen, Q. A novel tri-semicircle shaped submerged breakwater for mitigating wave loads on coastal bridges part I: Efficacy. *Ocean Eng.* **2022**, *245*, 110462. [[CrossRef](#)]
20. Ramesh, N.; Hegde, A.; Rao, S. Prediction of reflection coefficient of a perforated Quarter Circle Breakwater using artificial neural network (ann). *J. Phys. Conf. Ser.* **2019**, *1276*, 012006. [[CrossRef](#)]

21. Liu, Y.; Li, H.-J. Analysis of wave interaction with submerged perforated semi-circular breakwaters through multipole method. *Appl. Ocean Res.* **2012**, *34*, 164–172. [[CrossRef](#)]
22. Graw, K.U.; Knapp, S.; Sundar, V.; Sundaravadivelu, R. Dynamic pressures exerted on semicircular breakwater. *Leipz. Annu. Civ. Eng. Rep.* **1998**, *3*, 333–344.
23. Yuan, D.; Tao, J. Wave forces on submerged, alternately submerged, and emerged semicircular breakwaters. *Coast. Eng.* **2003**, *48*, 75–93. [[CrossRef](#)]
24. Tanimoto, K.; Namerikawa, N.; Ishimaru, Y.; Sekimoto, T. A hydraulic experimental study on semi-circular caisson breakwaters. *Port Harb. Res. Inst.* **1989**, *23*, 3–32.
25. Tanimoto, K.; Yoshimoto, N.; Namerikawa, N.; Ishimaru, Y. Hydraulic characteristics and design wave forces of semi-circular caisson breakwaters. *Coast. Eng. JSCE* **1987**, *34*, 551–555.
26. Tanimoto, K. Japanese experiences on composite breakwaters. In Proceedings of the International Workshop on Wave Barriers in Deepwaters, Yokosuka, Japan, 1 October 1994.
27. Zhang, N.-C.; Wang, L.-Q.; Yu, Y.-X. Oblique irregular waves load on semicircular breakwater. *Coast. Eng. J.* **2005**, *47*, 183–204. [[CrossRef](#)]
28. Le Xuan, T.; Ba, H.T.; Thanh, V.Q.; Wright, D.P.; Tanim, A.H.; Anh, D.T. Evaluation of coastal protection strategies and proposing multiple lines of defense under climate change in the Mekong Delta for sustainable shoreline protection. *Ocean Coast. Manag.* **2022**, *228*, 106301. [[CrossRef](#)]
29. Goda, Y.; Suzuki, Y. Estimation of incident and reflected waves in random wave experiments. In Proceedings of the Coastal Engineering 1976, Honolulu, HI, USA, 11–17 July 1976; pp. 828–845.
30. Teh, H.M.; Al-Towayti, F.A.H.; Venugopal, V.; Ma, Z. Interaction of Waves with a Free-Surface Semicircular Breakwater: Experimental Investigation and Empirical Models. *J. Mar. Sci. Eng.* **2023**, *11*, 1419. [[CrossRef](#)]
31. Roslan, M.N.A.B.; Teh, H.M.; Al-Towayti, F.A.H. Numerical Simulations of Wave Diffraction Around a Low-Crested Semicircular Breakwater. In *Proceedings of the 5th International Conference on Water Resources (ICWR)–Volume 1: Current Research in Water Resources, Coastal and Environment*; Springer: Berlin/Heidelberg, Germany, 2022.
32. Aburatani, S.; Koizuka, T.; Sasayama, H.; Tanimoto, K.; Namerikawa, N. Field test on a semi-circular caisson breakwater. *Coast. Eng. Jpn.* **1996**, *39*, 59–78. [[CrossRef](#)]
33. Sundar, V.; Ragu, V. Dynamic pressures and run-up on semicircular breakwaters due to random waves. *Ocean Eng.* **1998**, *25*, 221–241. [[CrossRef](#)]
34. SriKrishnapriya, M.; Roopsekhar, K.A.; Sundar, V.; Sundaravadivelu, R.; Graw, K.U.; Knapp, S. Hydrodynamic pressures on semi-circular breakwaters. In Proceedings of the 4th International Conference on Hydroscience and Engineering, Seoul, Republic of Korea, 26–27 July 2000.
35. Dhinakaran, G.; Sundar, V.; Sundaravadivelu, R.; Graw, K.U. Dynamic pressures and forces exerted on impermeable and seaside perforated semicircular breakwaters due to regular waves. *Ocean Eng.* **2002**, *29*, 1981–2004. [[CrossRef](#)]
36. Dhinakaran, G.; Sundar, V.; Sundaravadivelu, R.; Graw, K.U. Effect of perforations and rubble mound height on wave transformation characteristics of surface piercing semicircular breakwaters. *Ocean Eng.* **2009**, *36*, 1182–1198. [[CrossRef](#)]
37. Vijayalakshmi, K.; Neelamani, S.; Sundaravadivelu, R.; Murali, K. Wave runup on a concentric twin perforated circular cylinder. *Ocean Eng.* **2007**, *34*, 327–336. [[CrossRef](#)]
38. Nishanth, N. Hydrodynamic performance characteristics of semicircular breakwaters. Master’s Thesis, National Institute of Technology Karnataka, Surathkal, Mangaluru, India, 2008.
39. Köksal, G.; Batmaz, I.; Testik, M.C. A review of data mining applications for quality improvement in manufacturing industry. *Expert Syst. Appl.* **2011**, *38*, 13448–13467. [[CrossRef](#)]
40. Hegde, A.V.; Mohan, S.; Pinho, J.L.; Sharhabeel, P.S. *Physical Model Studies on the Stability of Emerged Seaside Perforated Semicircular Breakwaters*; NISCAIR-CSIR: Delhi, India, 2018.
41. Hakhoe, T.C. *International Journal of Naval Architecture and Ocean Engineering*; Society of Naval Architects of Korea: Seoul, Republic of Korea, 2009.
42. Nourani, O.; Askar, M.B. Comparison of the effect of tetrapod block and armor X block on reducing wave overtopping in breakwaters. *Open J. Mar. Sci.* **2017**, *7*, 472–484. [[CrossRef](#)]
43. Chen, Y.; Niu, G.; Ma, Y. Study on hydrodynamics of a new comb-type floating breakwater fixed on the water surface. In *E3S Web of Conferences*; EDP Sciences: Les Ulis, France, 2019.
44. Yang, H.Q.; Li, M.G.; Liu, S.X.; Zhang, Q.; Wang, J. A piston-type active absorbing wavemaker system with delay compensation. *China Ocean Eng.* **2015**, *29*, 917–924. [[CrossRef](#)]
45. Altomare, C.; Domínguez, J.M.; Crespo, A.J.C.; González-Cao, J.; Suzuki, T.; Gómez-Gesteira, M.; Troch, P. Long-crested wave generation and absorption for SPH-based DualSPHysics model. *Coast. Eng.* **2017**, *127*, 37–54. [[CrossRef](#)]
46. Yang, H.Q.; Li, M.G.; Liu, S.X.; Chen, F.M. An iterative re-weighted least-squares algorithm for the design of active absorbing wavemaker controller. *J. Hydrodyn. Ser. B* **2016**, *28*, 206–218. [[CrossRef](#)]
47. Schäffer, H.A. Some design aspects of an absorbing 3D wavemaker. In Proceedings of the Coastal Engineering 1998, Copenhagen, Denmark, 22–26 June 1998; pp. 1082–1095.
48. Grilli, S.T.; Horrillo, J.J. Numerical generation and absorption of fully nonlinear periodic waves. *J. Eng. Mech.* **1997**, *123*, 1060–1069. [[CrossRef](#)]

49. Teh, H.M.; Venugopal, V.; Bruce, T. Hydrodynamic characteristics of a free-surface semicircular breakwater exposed to irregular waves. *J. Waterw. Port Coast. Ocean Eng.* **2012**, *138*, 149–163. [[CrossRef](#)]
50. Al-Qadami, E.H.H.; Razi, M.A.M.; Damanik, W.S.; Mustafa, Z.; Martinez-Gomariz, E. Understanding the Stability of Passenger Vehicles Exposed to Water Flows through 3D CFD Modelling. *Sustainability* **2023**, *15*, 13262. [[CrossRef](#)]
51. Glatzel, T.; Litterst, C.; Cupelli, C.; Lindemann, T.; Moosmann, C.; Niekrawietz, R.; Streule, W.; Zengerle, R.; Koltay, P. Computational fluid dynamics (CFD) software tools for microfluidic applications—A case study. *Comput. Fluids* **2008**, *37*, 218–235. [[CrossRef](#)]
52. Yang, X.; James, A.J.; Lowengrub, J.; Zheng, X.; Cristini, V. An adaptive coupled level-set/volume-of-fluid interface capturing method for unstructured triangular grids. *J. Comput. Phys.* **2006**, *217*, 364–394. [[CrossRef](#)]
53. Al-Qadami, E.H.H.; Abdurraheed, A.S.I.; Mustafa, Z.; Yusof, K.W.; Malek, M.A.; Ab Ghani, A. Numerical modelling of flow characteristics over sharp crested triangular hump. *Results Eng.* **2019**, *4*, 100052. [[CrossRef](#)]
54. Hirt, C.W.; Nichols, B.D. Volume of fluid (VOF) method for the dynamics of free boundaries. *J. Comput. Phys.* **1981**, *39*, 201–225. [[CrossRef](#)]
55. Hirt, C.; Burkhudarov, M. Void regions and bubble models in Flow-3D. *Flow Sci. Rep.* **2013**, *1*, 1–13.
56. Al-Qadami, E.H.H.; Mustafa, Z.; Al-Atroush, M.E.; Martinez-Gomariz, E.; Teo, F.Y.; El-Husseini, Y. A numerical approach to understand the responses of passenger vehicles moving through floodwaters. *J. Flood Risk Manag.* **2022**, *15*, e12828. [[CrossRef](#)]
57. Cebeci, T. *Turbulence Models and Their Application: Efficient Numerical Methods with Computer Programs*; Springer Science & Business Media: Berlin/Heidelberg, Germany, 2003.
58. Mohammadi, B.; Pironneau, O. *Analysis of the k-Epsilon Turbulence Model*; Masson: Paris, France, 1993.
59. Patankar, S. *Numerical Heat Transfer and Fluid Flow*; CRC Press: Boca Raton, FL, USA, 2018.
60. Burcharth, H.; Hughes, S.A. Fundamentals of design. In *Coastal Engineering Manual*; Coastal Engineering Research Center: Fort Belvoir, VA, USA, 2003; pp. VI-5-1–VI-5-316.
61. Tien, N.A. Technology, To study impact level of dominant parameters and propose estimate methodology for wave transmission efficiency of unconventional complex submerged breakwater. *J. Mar. Sci. Technol.* **2019**, *19*, 611–625.
62. Ariyaratne, H.A.; Chang, K.A.; Lee, J.I.; Ryu, Y.U. Experimental study of flow fields around a perforated breakwater. *Int. J. Ocean Syst. Eng.* **2012**, *2*, 50–56. [[CrossRef](#)]
63. Kim, D.-H.; Koo, W.-C. Numerical Analysis of Hydrodynamic Performance of a Movable Submerged Breakwater Using Energy Dissipation Model. *J. Soc. Nav. Archit. Korea* **2012**, *49*, 287–295. [[CrossRef](#)]
64. Moragues, M.V.; Clavero, M.; Diaz-Carrasco, P.; Losada, M.A. Bulk dissipation and flow characteristics in cube armored breakwaters. *Coast. Eng. Proc.* **2020**, *36*, 40. [[CrossRef](#)]
65. Cheng, C.-L.; Garg, G.J. Coefficient of determination for multiple measurement error models. *J. Multivar. Anal.* **2014**, *126*, 137–152. [[CrossRef](#)]
66. Altowayti, W.A.H.; Othman, N.; Al-Gheethi, A.; Dzahir, N.H.b.M.; Asharuddin, S.M.; Alshalif, A.F.; Nasser, I.M.; Tajarudin, H.A.; AL-Towayti, F.A.H. Adsorption of Zn²⁺ from synthetic wastewater using dried watermelon rind (D-WMR): An overview of nonlinear and linear regression and error analysis. *Molecules* **2021**, *26*, 6176. [[CrossRef](#)] [[PubMed](#)]
67. Willmott, C.J.; Matsuura, K. Advantages of the mean absolute error (MAE) over the root mean square error (RMSE) in assessing average model performance. *Clim. Res.* **2005**, *30*, 79–82. [[CrossRef](#)]
68. Chai, T.; Draxler, R.R. Root mean square error (RMSE) or mean absolute error (MAE)?—Arguments against avoiding RMSE in the literature. *Geosci. Model Dev.* **2014**, *7*, 1247–1250. [[CrossRef](#)]
69. Schlurmann, T.; Bleck, M.; Oumeraci, H. Wave transformation at artificial reefs described by the Hilbert-Huang transformation (HHT). In *Coastal Engineering 2002: Solving Coastal Conundrums*; World Scientific: Singapore, 2003; pp. 1791–1803.
70. Nguyen, H.P.; Park, J.C.; Han, M.; Wang, C.M.; Abdussamie, N.; Penesis, I.; Howe, D. Representative transmission coefficient for evaluating the wave attenuation performance of 3D floating breakwaters in regular and irregular waves. *J. Mar. Sci. Eng.* **2021**, *9*, 388. [[CrossRef](#)]
71. Dhinakaran, G.; Sundar, V.; Sundaravadivelu, R.; Graw, K.U. Regular wave measurements on a submerged semicircular breakwater. *J. Offshore Mech. Arct. Eng.* **2010**, *132*, 034501. [[CrossRef](#)]
72. Mahmoudi, A.; Hakimzadeh, H.; Ketabdari, M.J.; Cartwright, N.; Vaghefi, M. Experimental study on wave transmission and reflection at impermeable submerged breakwaters. *Int. J. Coast Offshore Environ. Eng.* **2017**, *2*, 19–27.
73. Koraim, A.; Rageh, O. Hydrodynamic performance of vertical porous structures under regular waves. *China Ocean Eng.* **2013**, *27*, 451–468. [[CrossRef](#)]
74. Li, X.; Wang, Q.; You, J.; Guo, W.; Zhang, J.; Zhan, C.; Zhang, Z.; Wang, L.; Li, Q. Wave attenuation performance and the influencing factors of a lower arc-plate breakwater. *China Ocean Eng.* **2020**, *34*, 89–98. [[CrossRef](#)]
75. Teh, H.M.; Venugopal, V. Performance evaluation of a semicircular breakwater with truncated wave screens. *Ocean Eng.* **2013**, *70*, 160–176. [[CrossRef](#)]
76. Qi, Z.; Maxwell, P. Liquid Water: Ubiquitous Contributor to Aerosol Mass. *Environ. Sci. Technol. Lett.* **2016**, *3*, 257–263.
77. Fathi, A.; Ketabdari, M.J. Engineering, Modeling of emerged semi-circular breakwater performance against solitary waves using SPH method. *J. Braz. Soc. Mech. Sci. Eng.* **2018**, *40*, 290. [[CrossRef](#)]
78. Soares, C.G.; Cherneva, Z.; Antao, E. Steepness and asymmetry of the largest waves in storm sea states. *Ocean Eng.* **2004**, *31*, 1147–1167. [[CrossRef](#)]

79. Barzegar, M.; Palaniappan, D. Numerical study on the performance of semicircular and rectangular submerged breakwaters. *Ocean Syst. Eng.* **2020**, *10*, 201–226.
80. Young, D.M.; Testik, F.Y. Wave reflection by submerged vertical and semicircular breakwaters. *Ocean Eng.* **2011**, *38*, 1269–1276. [[CrossRef](#)]
81. Hegde, A.V.; Rao, S.; Kumar, K.J. Run-up, run-down and reflection characteristics of semicircular breakwater for varying seaside perforations. *ISH J. Hydraul. Eng.* **2012**, *18*, 145–151. [[CrossRef](#)]
82. Hegde, A.V.; Naseeb, S.M. Transmission performance of submerged semicircular breakwaters for different radii and submergence ratios. *Int. J. Ocean Clim. Syst.* **2014**, *5*, 151–161. [[CrossRef](#)]
83. Koutandos, E. Hydrodynamic analysis of a skirt breakwater. In *Proceedings of the Institution of Civil Engineers-Maritime Engineering*; Thomas Telford Ltd.: London, UK, 2007.
84. Günaydın, K.; Kabdaşlı, M. Performance of solid and perforated U-type breakwaters under regular and irregular waves. *Ocean Eng.* **2004**, *31*, 1377–1405. [[CrossRef](#)]
85. Günaydın, K.; Kabdaşlı, M. Investigation of II-type breakwaters performance under regular and irregular waves. *Ocean Eng.* **2007**, *34*, 1028–1043. [[CrossRef](#)]
86. Dhinakaran, G.; Sundar, V.; Sundaravadivelu, R.; Graw, K.U. Pressures on a seaside perforated semicircular breakwater. In *Proceedings of the International Conference in Ocean Engineering-2001, Madras, India, 11–14 December 2001*.

Disclaimer/Publisher’s Note: The statements, opinions and data contained in all publications are solely those of the individual author(s) and contributor(s) and not of MDPI and/or the editor(s). MDPI and/or the editor(s) disclaim responsibility for any injury to people or property resulting from any ideas, methods, instructions or products referred to in the content.